

NASA CR 156700

(NASA-CR-156700)	ALIGNMENT CONTROL STUDY	N78-20028
FOR THE SOLAR OPTICAL TELESCOPE	Final	
Report (Ball Bros. Research Corp.)	115 p HC	
A06/MF A01	CSCI 03A	Unclas
		07356

G3/89

ALIGNMENT CONTROL STUDY FOR THE SOLAR OPTICAL TELESCOPE

FINAL REPORT

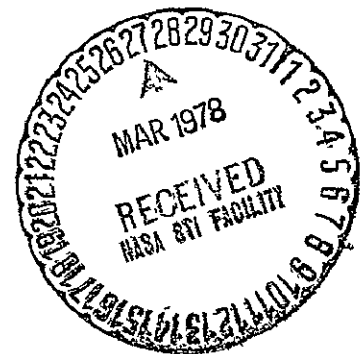
NAS5-23402, Mod No 2

OCTOBER 1976

Prepared By

BALL BROTHERS RESEARCH CORPORATION
BOULDER, COLORADO

Prepared For
GODDARD SPACE FLIGHT CENTER
GREENBELT, MARYLAND 20771



ALIGNMENT CONTROL STUDY

FOR THE
SOLAR OPTICAL
TELESCOPE

Final Report

October 1976

Prepared By

Ball Brothers Research Corp.
Boulder, Colo.
under Contract NAS5-23402, Mod. No. 2



FOREWORD

This report is submitted to Goddard Space Flight Center (GSFC) by Ball Brothers Research Corporation (BBRC) in response to NASA Contract Number NAS5-23402, Modification 2, for an Alignment Control Study of the Shuttle Optical Telescope (SOT).

Dr. W. M. Neupert is the GSFC Technical Officer and C. G. Stouffer is the Technical Monitor.

At BBRC, the study was conducted by Dr. M. Bottema, with the cooperation of R. H. Grunz (mechanical design), Dr. D. E. Regembrecht (thermal analysis) and R. J. Darnell (optical analysis).



INTRODUCTION

The purpose of this study is to develop concepts for alignment control of the Shuttle Optical Telescope (SOT).

The SOT is intended for solar, planetary and stellar observations from the Shuttle in a sortie mode. The basic concept for this telescope was developed by R. B. Dunn, leader of the SOT facility definition team (FDT). It consists of an $f/25.2$ gregorian system with an $f/3.6$ primary mirror and has the following unique features:

1. The telescope can be used alternatively for observations at the gregorian focus and the prime focus by interchanging the secondary mirror with two or more prime focus instruments.
2. The primary mirror can be articulated to implement bore-sighting with the SOT platform, rastering, offset pointing and alignment. In addition, the same control system may be used for image-motion compensation (IMC) at the prime focus.

In Dunn's concept, the main telescope structure is an aluminum truss, which carries not only the SOT and its complement of scientific instruments, but independent solar facilities as well. The structural ensemble is called the Long Pointed Spar (LPS), which is about 7 m long and has a diameter of about 3 m.

This study addresses itself to the question whether, in the above concept, alignment can be maintained or restored well enough to operate the telescope sufficiently close to its full angular resolution capability. This involves analysis of the alignment and focus errors that can be tolerated, methods of sensing such



errors and mechanisms to make the necessary corrections. Alternate approaches and their relative merits have also been considered.

The results of this study indicate that adequate alignment control can be achieved. It is recommended that additional analysis and experimental verification be conducted to better define the SOT alignment and control system.



CONTENTS

<u>Section</u>		<u>Page</u>
	FOREWORD	11
	INTRODUCTION	iii
1	STUDY OBJECTIVES	1-1
2	SUMMARY AND CONCLUSIONS	2-1
3	ALIGNMENT TOLERANCES	3-1
	3.1 IMAGE FORMATION IN PERFECT TELESCOPE	3-2
	3.2 ALIGNMENT ERRORS AND ASSOCIATED ABERRATIONS	3-8
	3.3 TOLERANCE CRITERIA	3-11
	3.4 MODULATION TRANSFER CHARACTERISTICS	3-14
4	THERMAL EFFECTS ON ALIGNMENT	4-1
	4.1 THERMAL ENVIRONMENT OF TRUSS STRUCTURE	4-1
	4.2 TRUSS RESPONSE TO INTERMITTENT INSOLATION	4-2
	4.3 RECOMMENDED FOCUS AND CENTERING UPDATE INTERVALS	4-8
5	ALIGNMENT SENSING	5-1
	5.1 FOCUS SENSING AT GREGORIAN FOCUS	5-2
	5.2 CENTERING SENSING IN GREGORIAN TELESCOPE	5-19
	5.3 FOCUS AND CENTERING SENSING IN PRIME-FOCUS MODE	5-25
	5.4 ACCOMMODATION OF ALIGNMENT SENSING SYSTEMS	5-29
6	PRIMARY MIRROR CONTROL MECHANISMS	6-1
	6.1 A-FRAME MOTIONS AND FORCES	6-2
	6.2 INSERTS IN PRIMARY MIRROR	6-9
	6.3 ACTUATORS	6-27
	REFERENCLS	A-1



1.0 STUDY OBJECTIVES

The purpose and scope of the present study were formulated by GSFC as follows.

The purpose of the ACS study is to determine the feasibility of, and define a subsystem concept for, active alignment control of the optical system for the one-meter VIS/UV telescope. The goal is to provide near diffraction limited performance during orbital observations from a Space Shuttle Orbiter/Spacelab vehicle during a seven to thirty day sortie mission.

Specifically, the contractor shall develop a baseline optical misalignment budget resulting from thermal distortions for 1.0 and 1.25 meter telescope systems and develop an alignment control concept. The misalignment budget shall be made for a worst case example, considering both a full sunlit orbit and a day/night cycle orbit, with the telescope operating either as a solar instrument or as a stellar instrument (full orbits of operation in one or the other mode).

Using this misalignment error budget, the contractor shall define an optimum method for alignment control of the telescope with the goal of maximizing the period of orbital time that shall be available at diffraction limited performance and the ease of providing access to the prime focus for a number of instruments. Preliminary studies indicate that control of the primary mirror will simplify operation of prime focus instrumentation so this approach should be included in the contractor's study. Analysis shall include problems of achieving and maintaining alignment, focus and image stability. The study shall assume current nominal specification of tracking error inputs and bandwidth from the ESA Instrument Pointing System (IPS). Problems of boresighting with



the additional instruments shall be included. Preliminary engineering designs of a mirror mount, including attachment to a solid mirror of either 1.0 or 1.25 meter aperture shall be provided. Such designs will include mirror launch and landing loads as well as any mirror figure control required during preflight testing and in-orbit operations.

In this study, the optical design to be baselined is the telescope specified by the Solar Physics One-Meter Telescope Facility Definition team. However, for each subsystem or technological area studied, the contractor shall identify areas of major engineering impact that are the result of increasing the aperture of the telescope from 1.0 to 1.25 meters, the focal length being the same for these two cases. A table of cost ratios for the subsystems that are studied for the two sizes of telescope shall be assembled.

A previous study of cluster concepts for GSFC, called the Long Pointed Spar (LPS) Study, will provide baseline data for the ACS study. The LPS study resulted in a concept for the VIS/UV telescope which provides an integrating structure for a cluster of solar instrument facilities. The LPS study results are contained in BBRC Final Report F76-15, dated April, 1976.

The LPS structure and thermal control concepts will be used as a baseline for the ACS study. The additional instrument facilities as defined in the LPS study will also be assumed in order to evaluate their effects on distortions of the structure.



2.0 SUMMARY AND CONCLUSIONS

The Shuttle Optical Telescope (SOT) is conceived as a multiple-purpose telescope for observations from the Shuttle during a sortie mission. The SOT is designed primarily for solar observations, but can also be applied to planetary and stellar work. It permits two modes of operation; i.e., the scientific instruments (cameras, spectrographs, etc.) can be placed either at the gregorian focus (Figure 2-1A) or at the prime focus (Figure 2-1B).

The purpose of this study is to devise means by which the image quality in either mode of operation can be maintained at the highest possible level after the SOT has passed through launch and deployment and is exposed to the orbital environment.

In the gregorian mode of operation, conservation of image quality requires first of all that the telescope remains in focus, i.e., the axial separation Δf between the telescope image and the detector or instrument slit ("defocus" in Figure 2-1A) must be kept within small tolerances. This can be controlled by axial displacement of the primary mirror, i.e., by adjustment of the object distance F_1S of the prime focus with respect to the secondary mirror. The axial displacement of F_1 from its nominal position will be called "despace" and is labeled as such in Figure 2-1A.

A second, but less stringent, requirement for high image quality at the gregorian focus is that F_1 lies close to the optical axis of the secondary mirror. The deviation is called "decenter" and can be controlled by lateral displacement of the primary mirror and/or tilt around its vertex.

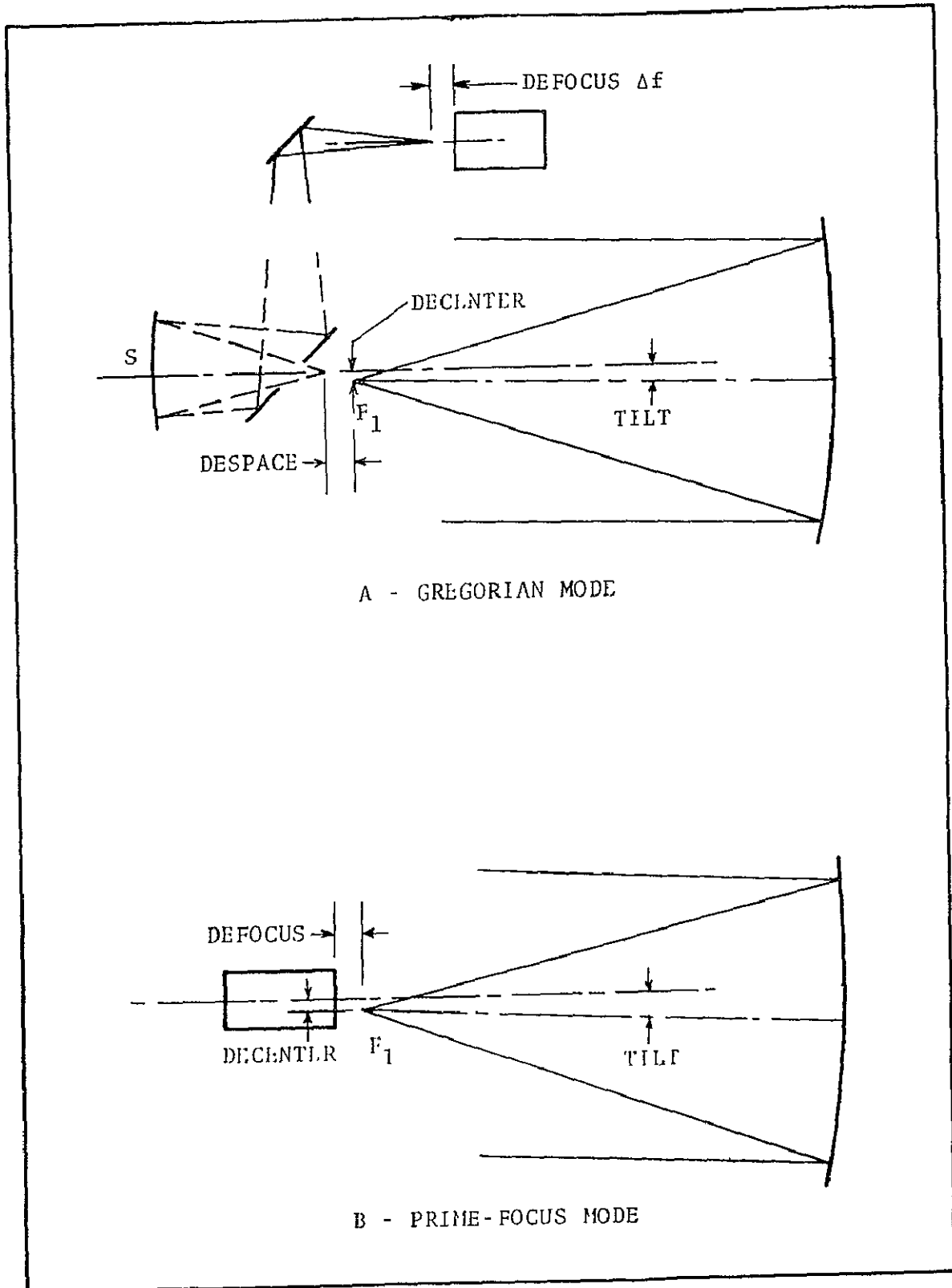


Figure 2-1 SOT modes of operation



If despace and decenter are both sufficiently small, the primary mirror can be tilted around F_1 as a center without degrading the image quality at the gregorian focus. This makes it possible to use primary mirror tilts up to 1° or more for offset pointing and rastering.

In the prime-focus mode of operation, defocus and decenter (Figure 2-1B) relate directly to the location of the prime focus with respect to the prime-focus instrument. Both are controlled by articulation of the primary mirror. Here too, offset pointing by rotation of the primary mirror around F_1 is feasible.

The specific problems addressed in this report are:

1. Derivation of reasonable tolerances for defocus, despace and decenter, in relation to other factors controlling image quality; i.e., mirror imperfections and diffraction (Section 3).
2. Analysis of alignment disturbances caused by changes in thermal environment in alternate solar and stellar observations (Section 4).
3. Concepts for alignment-error sensing devices (Section 5).
4. Mechanisms for alignment correction by control of the primary mirror (Section 6).

Each of these is summarized below, together with the most important conclusions with regard to further developments of the SOT.

ORIGINAL PAGE IS
OF POOR QUALITY



Tolerances. Alignment tolerances for the gregorian mode of operation were derived by comparing wavefront errors, caused by misalignment, to figure errors in high-quality mirrors. This led to the following criteria:

	<u>Design Goals</u>	<u>Acceptable Maxima</u>
Defocus	<u>+250</u> μm	<u>+500</u> μm
Despace	<u>±</u> 5 μm	<u>±</u> 10 μm
Decenter	75 μm	150 μm

The most critical parameter is defocus. The reason is that small focus errors are difficult to detect, but introduce relatively large wavefront errors. The proposed maximum tolerance was justified by evaluation of the MTF characteristics at a few wavelengths between 110 nm and 660 nm, assuming figure errors of 0.01 μm rms ($\lambda/64$ rms at 633 nm) on both mirrors. An interesting additional conclusion from this work is that angular resolutions of the order of 0.1" are feasible only if mirrors of the above extreme high quality are used and then only in a limited spectral interval in the near UV.

For the prime-focus mode, an angular resolution of 0.5" seems sufficient. The corresponding tolerances are ±50 μm for defocus and 0.5 mm for decenter.

Thermal Effects. On-orbit, the most severe alignment disturbances stem from changes in thermal environment in alternate solar and stellar observations. Despace, in particular, is highly sensitive to temperature fluctuations in the aluminum truss structure. The largest acceptable tolerance corresponds to an overall temperature change of only ±0.08°C. However, this study shows that sufficient temperature stabilization may be feasible if (1) the truss longerons are well isolated, (2) solar radiation is not admitted.



until the LPS is centered on the sun and (3) solar heating is simulated during stellar observations. This presupposes that the LPS is surrounded by a thermal shroud, held at 10°C , with no greater temperature differentials than $\pm 3^{\circ}\text{C}$. The analysis was restricted to highly simplified calculations of radiative heat exchange only. These suggest that focus updates would be needed only every 20 min. However, conductive effects might reduce this number considerably. On this basis, this study estimates that focus updates may be needed every few minutes and decenter updates, which are far less critical, every half hour. This assumes that correction within a small fraction of the tolerance is feasible, so that the major part of the tolerance can be left to uncontrolled drift.

For future SOT developments, close coordination of thermal and mechanical design is strongly recommended. Local and variable heat inputs (e.g., from mechanisms) should carefully be avoided to maintain update intervals of the above magnitudes.

Defocus Detection at the Gregorian Focus. This study recommends sensing by means of two laser beams, which traverse the telescope twice in opposite directions. A laser diode and a detector (quadrant silicon photodiode) are located near the gregorian focus. The beams follow a path that lies outside the telescope beam at the primary mirror and fully clears the heat-rejection system. The present reliably predictable accuracy is only $200\text{ }\mu\text{m}$ rms, which would mean that almost continuous update of focus is necessary (e.g., every few seconds). However, it appears that an actual accuracy of about $80\text{ }\mu\text{m}$ is possible. This would suffice to allow a few minutes free drift.



As an alternative, this study considers a three-beam interferometric sensing device, which compares the optical path length at the extreme edge of the telescope beam to that through the center. The accuracy easily exceeds 1/10 of the 250 μm focus-tolerance goal, but the range is only about ± 1 mm. This method becomes of interest only if further analysis or, preferably, experiments show that no improvement of the first method is possible.

Decenter Detection in Gregorian Mode. Decenter is detected by means of two reimaging projectors, mounted to the back side of the primary mirror. Laser beams, projected from the periphery of the primary mirror, pass through the prime focus to reflectors at the edge of the secondary mirror and back to quadrant silicon sensors in the projectors. These provide X and Y decenter error signals and also a crude measurement of despace. The latter is valuable for initial alignment on-orbit. Decenter errors, equal to 1/10 of the tolerance, can easily be detected.

Defocus and Decenter Detection in Prime-Focus Mode. For prime-focus instruments, focus and centering errors are detected simultaneously by means of offset beams in the above projectors. Each prime-focus instrument has its own set of sensors, which are placed about 80 mm off-axis, to clear the heat-rejection mirror. The detectable centering errors are only a minute fraction of the decenter tolerance, but the calculated detectable focus errors appear to be of the same order as the focus tolerance. In practice, better detection may be possible, however. Also, for prime-focus observations, the primary mirror controls must remain active to provide image-motion compensation, which permits continuous focus updates.

ORIGINAL PAGE IS
OF POOR QUALITY



Recommendations for Alignment Sensing. Experimental tests of the above and alternate sensing methods are highly recommended for future SOT developments. These could be expanded to include breadboarding of the complete servo-control loop.

Alignment Control Mechanism. The section on control mechanisms and mounting of the primary mirror is devoted mainly to the "A-frame" concept, proposed by R. B. Dunn. This consists of 6 linear actuators, attached to 6 equally spaced points at the periphery of the mirror. By means of universal joints, the actuators are linked to inserts, which are mounted directly into the mirror blank and secured by elastic locking rings. This study analyzes the following aspects of this concept:

- Motions of the A-frame, necessary for specific alignment adjustments
- Actuator tolerances corresponding to the various alignment tolerances
- Mechanical properties of the elastically locked insert, in particular, its stiffness
- Stresses induced in the mirror blank during operation on-orbit, launch and landing, and preflight testing
- An alternate insert concept, using hard-point mounting.

Significant conclusions are:

1. The elastic insert offers less stiffness than hard-point mounting, but dependent upon the design, may induce higher stresses in the blank.
2. The elastic insert can be optimized for use on-orbit, but is not suitable for preflight testing. The hard-mounted insert can safely be applied in vertical testing on the ground.
3. Launch locks are necessary during launch and landing.



4. During observations, actuator forces may possibly disturb the mirror figure. Detailed stress analysis by computer or actual testing is necessary to resolve this question.

With regard to actuator mechanisms, various concepts were evaluated early in the study. Discussions at the mid-term review led to the selection of a specific approach, based on a ball-bearing screw, driven by a harmonic drive. A detailed design was subsequently prepared by R. B. Dunn and is included in this report.

For coupling of the actuator to the insert, this study recommends a ball-bearing joint, which can be decoupled during launch by means of the launch-lock mechanism.

The general conclusion with regard to mirror mounts and control mechanisms is that more analysis, including modeling, is necessary before a specific approach can be recommended. This study fully supports the idea of engineering tests planned by the FDT.



3.0 ALIGNMENT TOLERANCES

The factors that control the image quality in a space telescope can be divided into three categories:

1. Diffraction by the telescope aperture and any obscurations within the aperture.
2. Optical quality of the telescope, i.e.
 - Degree of correction of aberrations
 - Exactness of mirror surfaces.
3. Environmental effects, i.e.
 - Alignment and focus errors induced by the thermal environment on-orbit and by launch
 - Residual image motion caused by pointing disturbances.

For sufficiently long wavelengths, diffraction masks all other effects. The telescope performance is said to be diffraction-limited and the angular resolution (i.e., the smallest detectable separation δ between two point sources) is given by the classical relation

$$\delta = 1.22 \lambda / (2r) \quad (3.0)$$

where λ is the wavelength and $2r$ the diameter of the entrance pupil, i.e., the primary mirror. For the SOT, it may be expected that diffraction-limited performance is feasible in the visible. However at smaller wavelengths (i.e., in the near and middle UV), the quality of the optics and the environmental effects gradually take over as the factors limiting the image quality. Below a certain wavelength, Eq. (3.0) is no longer valid and the image quality does not further improve.



The question arises, how to establish criteria for alignment and focus tolerances under the above conditions. This is done by comparison of the wavefront deviations caused by alignment and focus errors to those associated with the non-reduceable mirror imperfections. The tolerances, so derived, are equivalent to those in a telescope, diffraction-limited at about 400 nm. The selection of these tolerances is further justified by a study of the corresponding effects on the modulation transfer function (MTF) at various UV wavelengths.

Before defining the above tolerances, this section first establishes the telescope parameters used in this study, and also derives the geometrical aberrations and wavefront deviations associated with the alignment errors of interest.

3.1 IMAGE FORMATION IN PERFECT TELESCOPE

We first consider a perfectly aligned telescope with perfect mirrors. A diagram is shown in Figure 3-1 and numerical data for the SOT parameters used in this study are listed in Table 3-1. These closely follow R. B. Dunn's definition (Ref. 3.1), but a small adjustment in the secondary focal length has been made to create a round number value for the short conjugate distance. Conrady's sign convention is followed.

The primary mirror is a paraboloid and provides exact stigmatic imaging at the prime focus. However, the usable field at the prime focus is strongly limited by third-order coma. The angular diameter in the radial direction is

$$\eta_c = (3/4)(r/f_1)^2 \alpha \quad (3.1)$$

where α is the field angle. This aberration already exceeds 0.5" for $\alpha = 35''$.

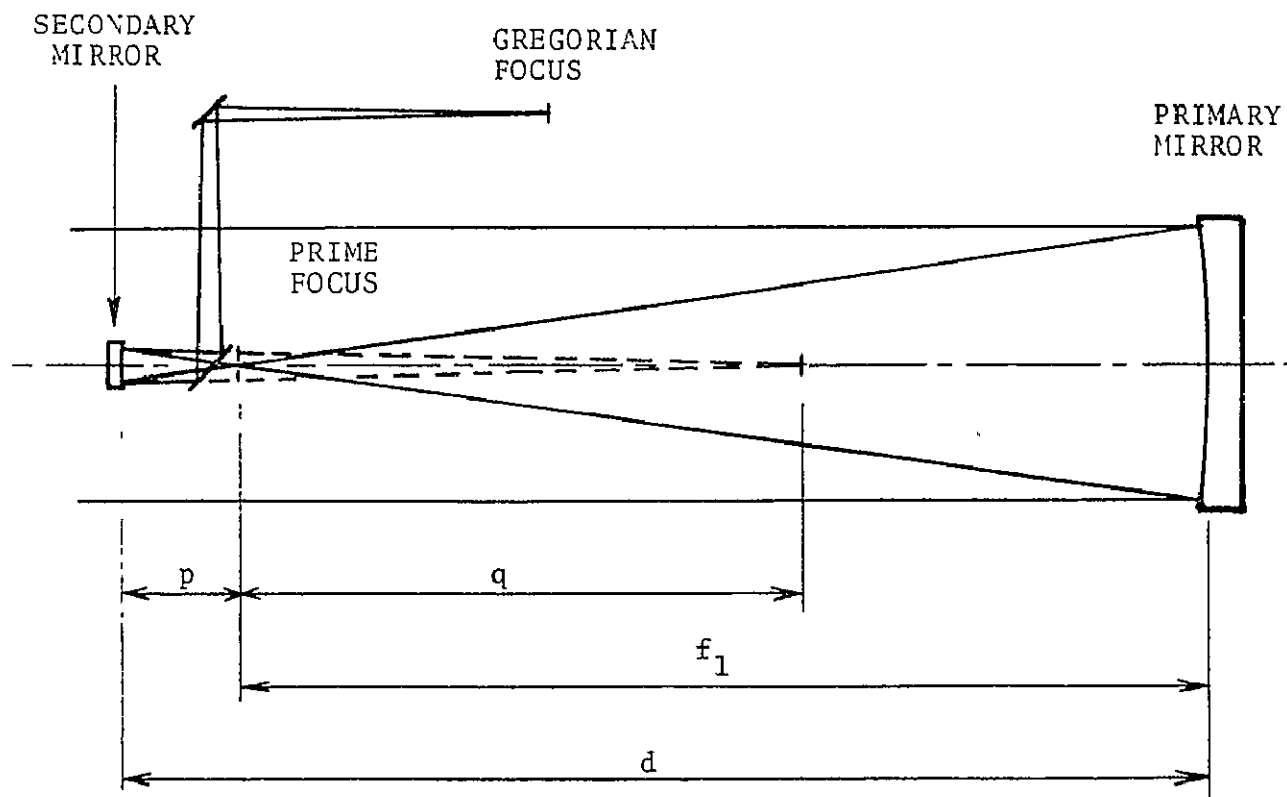


Figure 3-1 Optical diagram of SOT



Table 3-1
SOT OPTICAL PARAMETERS

Telescope

focal length	f	=	-31500	mm
diameter entrance stop	$2r$	=	1250	mm
f number	$F\#$	=	25.2	

Primary Mirror (paraboloid)

focal length	f_1	=	- 4500	mm
conic constant	$e_1 - 1$	=	- 1	
f number	$F_1\#$	=	3.6	

Mirror Separation

d	=	- 4957.2	mm
-----	---	----------	----

Secondary Mirror (ellipsoid)

focal length	f_2	=	400.05	mm
conic constant	$e_2 - 1$	=	- 0.5625	
object distance	p	=	- 457.2	mm
image distance	q	=	3200.4	mm
secondary magnification	m	=	- 7	
axial height ratio*	γ	=	- 0.1016	
back-focal ratio	s	=	0.6456064	

Pupils

exit/entrance pupil height ratio**	μ	=	- 0.0877851	
exit pupil/image distance	u	=	2765.23	mm

* In Ref. 3.2, this is incorrectly called the obscuration ratio.

**Entrance stop at primary mirror. $\mu = \gamma m / (m - 1 + \gamma)$
 $u = \mu f$



The secondary mirror is an ellipsoid and provides exact stigmatic imaging at the gregorian focus.

The telescope field-of-view has a diameter of 6'. This corresponds to a field diameter of 55 mm at the gregorian focus. As a result of the high secondary magnification, this field is strongly curved. In addition, there is some third-order coma and astigmatism.

There are three ways to correct for the curved field and aberrations:

1. The detector is curved to match the mean curvature of field,
2. A flat detector is placed at "best" focus, which lies about 0.45 mm behind the paraxial focus,
3. Field curvature and aberrations are eliminated by refractive correctors.

The first solution is applicable to electrography in the UV, for instance. The remaining aberrations are negligible. The second solution is unsatisfactory, because both the image blur on axis and at the edge of the field are so large that no margin is left for focus errors induced by the telescope environment. The third solution is the preferred. In the total image-quality budget, maximum allowance can then be made for alignment errors. Also, alignment tolerances, derived for zero field angle, can then be applied to the entire field. In the following sections, we will assume that this condition has been fulfilled.

Equations and numerical data for the calculation of the aberrations in the above three cases are given in Table 3-2. The total aberrations are shown in Figure 3-2. Comparison with exact ray

Table 3-2
THIRD-ORDER ABERRATIONS IN VARIOUS IMAGE
PLANES AT GREGORIAN FOCUS

		<u>Gaussian</u>	<u>Curved</u>	<u>"Best" Flat</u>
Radial Direction:				
$\eta = A_2 (r/f)^2 \alpha (2 + \cos 2\theta)$	coma	•	•	•
$+ A_3 (r/f) \alpha^2 \cos \theta$	astigmatism	•	•	•
$+ (A_3 + A_4) (r/f) \alpha^2 \cos \theta$	curvature	•		•
$+ (\Delta f/f) (r/f) \alpha^2 \cos \theta$	defocussing			•
$+ A_5 \alpha^3$	distortion			
Tangential Direction:				
$\xi = A_2 (r/f)^2 \alpha \sin 2\theta$	coma	•	•	•
$- A_3 (r/f) \alpha^2 \sin \theta$	astigmatism	•	•	•
$+ (A_3 + A_4) (r/f) \alpha^2 \sin \theta$	curvature	•		•
$+ (\Delta f/f) (r/f) \alpha^2 \sin \theta$	defocussing			•

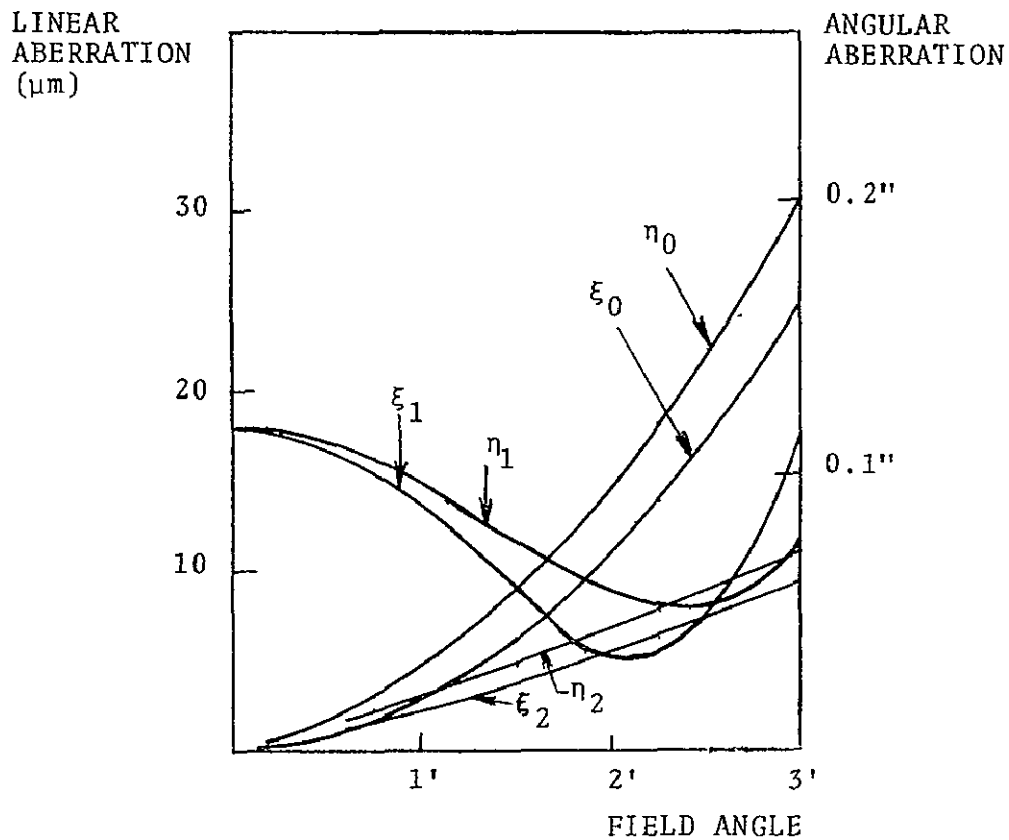
ABERRATION CONSTANTS

$$\begin{aligned}
 A_2 &= -0.25 \\
 A_3 &= -(m + s - 1)/(2s) = 5.6957 \\
 A_4 &= -(m^2 - 1)/(2s) = -37.174 \\
 A_5 &= -35.592
 \end{aligned}$$

RADII OF CURVATURE (mm)

$$\begin{aligned}
 \text{Sagittal} \quad r_s &= (1/2)f/A_4 = 423.68 \\
 \text{Tangential} \quad r_t &= (1/2)f/(2A_3 + A_4) = 610.87 \\
 \text{Mean} \quad r_m &= (1/2)f/(A_3 + A_4) = 500.34 \\
 \text{Petzval} \quad r_p &= (1/2)f/(-A_3 + A_4) = 367.39
 \end{aligned}$$

For interpretation of these equations, see Reference 3.2.



ξ_0, η_0 Gaussian, flat
 ξ_1, η_1 Best-focus, flat
 ξ_2, η_2 Mean-curved

ξ and η are the total image blurs in the tangential and radial directions, respectively.

Figure 3-2 Geometrical aberrations in 3 image planes at the gregorian focus
 ORIGINAL PAGE IS
 OF POOR QUALITY



tracings by means of the ACCOS V computer program shows that higher-order aberrations are entirely negligible in the 6' field. The third-order approximation is, therefore, fully justified. This also applies to the analysis in the following sections.

3.2 ALIGNMENT ERRORS AND ASSOCIATED ABERRATIONS

The approach to alignment control is based on the fact that no aberrations are introduced in the telescope image, if the prime focus and the first conjugate remain coincident. We note that this applies to stigmatic configurations of cassegrain and gregorian telescopes only and not, for instance, to the aplanatic versions. This means that large tilts of the primary mirror with respect to the secondary mirror (considered fixed) are permitted. On the SOT, this allows offset pointing with respect to the LPS by as much as a full sun diameter. However, there is a restriction on usable field, as will be discussed in Section 3.2.3.

In view of the above, the only significant alignment errors are:

- Despace, an error in the mirror separation,
- Defocus, a mismatch between the location of the image plane and the gregorian focus,
- Decenter, a lateral separation between the prime focus and the first conjugate of the secondary mirror.

Each of these is discussed in detail below.

3.2.1 Despace and Defocus

Despace is caused by thermal changes in the telescope structure and in the mirror mounts. An error Δd produces a change in image distance $\Delta q \approx m^2 \Delta d$, relative to the secondary mirror, which constitutes the most important contribution to the focus error at the gregorian focus.



A small focus error has a relatively large impact on image quality but is difficult to detect (Section 5). Therefore, defocus and despace are the most serious alignment errors to contend with.

A focus error Δf introduces an angular aberration $(\Delta f/f)(r/f)$, which can be interpreted as originating from a wavefront deviation at the entrance pupil, given by

$$s_{\Delta f} = (1/2)\Delta f(r/f)^2 \quad (3.2)$$

This wavefront deviation will be used later to establish despace and defocus tolerances (Section 3.3).

The image at the gregorian focus is kept focussed by adjustment of the mirror separation only. This means that changes in the secondary image distance are compensated by intentional despace. For extremely large image-distance errors (several mm), this procedure would introduce aberrations (mostly third-order spherical), but these are highly unlikely in the SOT.

3.2.2 Decenter

Decenter causes a first-order lateral displacement of the telescope image and also introduces third-order coma. The first-order effect makes it easy to detect decenter but does not affect the telescope image if image-motion compensation is applied. Since the effect on image quality is only of the third order, relatively large decenter errors are acceptable. Hence, centering is comparatively easy to control.



If the telescope image is fully corrected, the decenter-induced coma is the same throughout the whole field. Relative to the decenter direction as the Y axis, the coma is described by

$$\eta_{\Delta, \text{coma}} = (1/4)m(m^2 - 1)(\Delta/f)(r/f)^2(2 + \cos\theta) \quad (3.3)$$

$$\xi_{\Delta, \text{coma}} = (1/4)m(m^2 - 1)(\Delta/f)(r/f)^2 \sin 2\theta \quad (3.4)$$

where Δ is the decenter distance. The associated wavefront deviation is given by

$$s_{\Delta, \text{coma}} = (1/4)m(m^2 - 1)\Delta(r/f)^3 \cos\theta. \quad (3.5)$$

If the telescope image is not corrected, the above coma is superimposed upon the coma already present. The result is a coma-free point of a field angle

$$\alpha_{\Delta} = m(m^2 - 1)\Delta/f \quad (3.6)$$

in the direction of decentering. The composite coma is distributed circularly symmetrical around this point. However, for the establishment of a decenter tolerance, we will only concern ourselves with the fully corrected case. Decenter has no effect on astigmatism and curvature, but small tilts of the sagittal and tangential image planes are introduced. The corresponding image blurs in the image plane are smaller than coma by a factor of the order Δ/f and are, therefore, entirely negligible in the present case.

3.2.3 Tilt of Primary Mirror

The paraxial effect of a primary-mirror tilt τ is a tilt $m\tau$ of the gregorian image plane. This causes a defocussing, as a function of the field angle α , equal to



$$\Delta f_{\tau} = m\alpha r f. \quad (3.7)$$

This places a serious constraint on the usable field as a function of τ . If we assume a maximum permitted focus error $\Delta f_{\tau} = 0.25$ mm as part of the focal tolerance budget, we find, for instance, that the full field ($\alpha = 3'$) cannot be offset by more than $4.5'$. Conversely, if the offset is a full sun diameter ($\tau = 32'$), the usable field diameter is only $0.8'$.

In addition to the paraxial effect, small tilts are introduced as a result of the decentering of the telescope beam at the secondary mirror. These are different for the sagittal and tangential image planes, but are all smaller than the paraxial effect by a factor, roughly equal to m , and may be ignored.

3.3 TOLERANCE CRITERIA

At the inception of the study, R. B. Dunn put forward tolerance requirements for defocus and decentering, based on the Rayleigh criterion ($\lambda/4$ maximum wavefront error) at 100 nm, the shortest wavelength of interest. This led to a focal tolerance of ± 125 μ m at the gregorian focus, corresponding to a despace tolerance of ± 2.5 μ m, and a decenter tolerance of 38 μ m. These tolerances would be meaningful if the telescope performance at 100 nm were limited by diffraction. Even with the best modern mirror-figuring techniques, this cannot be achieved. In addition, the efficiency of the telescope is so low at 100 nm, that only the prime focus is of practical interest, where the angular resolution is detector limited to $0.5''$ at the very best.

Adherence to the above tolerances would seriously impact the cost and complexity of the alignment control systems. Therefore, this study proposes to relax the tolerances by a factor of 4, which



corresponds to application of the $\lambda/4$ criterion at 400 nm. The diffraction limited resolution at this wavelength is 0.10" for a 100 cm diameter telescope and 0.08" for a 125 cm diameter telescope. However, as a contingency, we maintain a design goal of only twice Dunn's criteria. Hence, the alignment tolerances for this study become:

	Design Goal	Acceptable Maximum
Focus Tolerance Δf	$\pm 250 \text{ } \mu\text{m}$	$\pm 500 \text{ } \mu\text{m}$
Despace Tolerance Δd	$\pm 5 \text{ } \mu\text{m}$	$\pm 10 \text{ } \mu\text{m}$
Decenter Tolerance Δ	$75 \text{ } \mu\text{m}$	$150 \text{ } \mu\text{m}$

The effect on alignment errors of the above magnitude may be assessed in terms of their contributions to the total rms wavefront error in the telescope. A major part of the wavefront error budget is taken up by residual mirror surface errors. These consist of a few undulations, spread across the mirror area. For modern mirrors, the surface deviations may be as small as $\lambda/70$ rms of the test wavelength, which is usually the 633 nm laser line (Ref. 3.3, 3.4). For a two mirror system (not counting the folding mirrors), the compound wavefront error then amounts to 0.026 μm rms.

The rms wavefront error corresponding to the focus tolerance can be calculated from Eq. (3.2) by averaging $s_{\Delta f}^2$ over the entrance pupil. We find

$$s_{\Delta f, \text{rms}} = (1/12) \sqrt{3} \Delta f (r/f)^2 \quad (3.8)$$

or, numerically,

Δf	$s_{\Delta f, \text{rms}}$
$\pm 250 \text{ } \mu\text{m}$	0.014 μm
$\pm 500 \text{ } \mu\text{m}$	0.029 μm



From Eq. (3.5), the rms wavefront error, introduced by decentering, is found to be

$$s_{\Delta, \text{rms}} = (1/48) \sqrt{2} m(m^2 - 1) \Delta (r/f)^3 \quad (3.9)$$

For the above tolerances, this becomes

Δ	$s_{\Delta, \text{rms}}$
75 μm	0.006 μm
150 μm	0.012 μm

The decenter wavefront error is far less than the defocus error, if both are based on the same $\lambda/4$ criterion. This might be a consideration to increase the decenter tolerance, but this does not make sense, since centering can relatively easily be controlled. As far as alignment errors are concerned, the major part of the budget must simply be left to focussing errors. This is also the procedure followed in Reference 3.3.

The total wavefront error in the presence of the largest alignment errors and realistic figure errors is 0.041 μm rms or $\lambda/15$ at 633 nm, which is still considered acceptable for diffraction limited performance at this wavelength.

With regard to alignment error sensing and correction, the policy in this study is to aim for an accuracy corresponding to a small fraction of the tolerance. The major part of the tolerance then remains available for drift between corrections.



3.4 MODULATION TRANSFER CHARACTERISTICS

The angular resolution capability of the telescope is best described by its modulation transfer function (MTF). In the case at hand, the two major points of interest are: (1) the changes in the MTF as a function of wavelength, and (2) the effect of focus errors. The latter is of importance with regard to the maximum acceptable focus error, established in Section 3.3. Because centering errors can easily be controlled, their effect on the MTF will be ignored here.

In general, figure errors form a smooth, undulatory pattern on the mirror surface. Although computer simulation of a two-dimensional figure error distribution is possible, we restrict ourselves here to a rotationally symmetrical distribution. This suffices for the present purpose and has the advantage that the MTF becomes independent of the azimuth around the telescope axis.

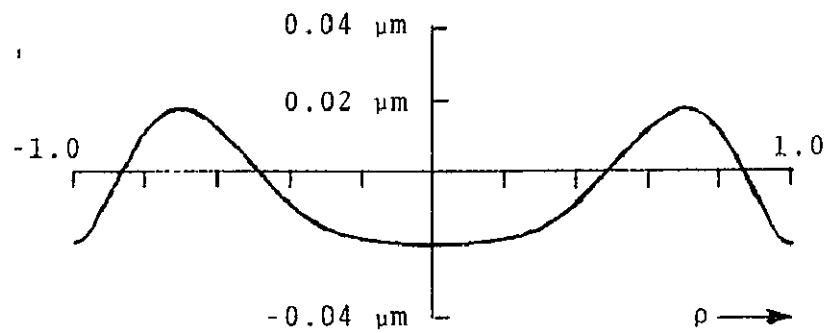
The numerical calculation of the MTFs was done by means of the ACCOS-V computer program. Five wavelengths between 661 nm and 110 nm were selected and three image positions, i.e., gaussian focus, 0.5 mm inside focus and 0.5 mm outside focus. In all cases, perfect centering, zero field angle and an obscuration ratio $\beta = 0.12$ were assumed.

The wavefront error was simulated by higher-order aspherics on the primary mirror only. For the secondary mirror, a perfect conic section was maintained. Two different primary mirror figure error profiles were examined. One is of the 8th order (Curve A, Figure 3-3) and the other of the 10th order (Curve B, Figure 3-3). As a function of the relative height $\rho = r/r_0$ in the entrance pupil, profile A is represented by

$$R(\rho) = 0.02 (30\rho^8 - 60\rho^8 + 30\rho^4 - 1) \mu\text{m} \quad (3.10)$$

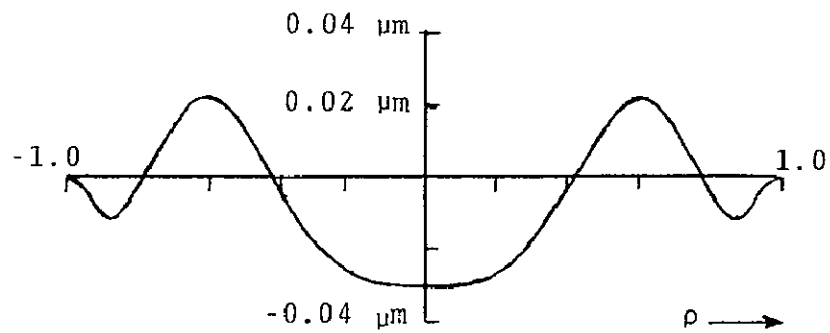


A



$$R(\rho) = 0.02 (30\rho^8 - 60\rho^6 + 30\rho^4 - 1) \mu\text{m}$$

B



$$R(\rho) = 0.03 (84\rho^{10} - 225\rho^8 + 200\rho^6 - 60\rho^4 + 1) \mu\text{m}$$

Figure 3-3 Model figure-error distribution functions



This function was constructed as the composite of two circle polynomials (Ref. 3.5), i.e.

$$R(\rho) = 0.02[(3/7)R_8^0(\rho) - (10/7)R_4^0(\rho)] \mu\text{m} \quad (3.11)$$

where

$$R_8^0(\rho) = 70\rho^8 - 140\rho^6 + 90\rho^4 - 20\rho^2 + 1 \quad (3.12)$$

and

$$R_4^0(\rho) = 6\rho^4 - 6\rho^2 + 1 \quad (3.13)$$

These polynomials represent compensated 7th and 3rd order spherical-aberration terms, respectively, and were combined, in the manner shown, to cancel the ρ^2 term, which cannot conveniently be introduced in the computer program separately. Also, this combination is the simplest one possible for which $dR/d\rho = 0$ for $\rho = 1$. This condition was found to be desirable to reduce computer wavefront sampling errors at the edge of the pupil.

If the wavefront aberrations are introduced by means of circle polynomials, the diffraction focus (i.e., maximum axial irradiance location) remains at the gaussian focus, because the average wavefront deviation is zero. However, this is true only if the aperture is unobscured. In the present case, a shift of 0.030 mm occurs. This is small enough to be ignored.

The rms value of $R(\rho)$ can be readily calculated from Eq.(3.11) by use of the orthogonality relations of the circle polynomials (Ref. 3.5). For the coefficients selected for Eq.(3.11), we then find $R_{\text{rms}} = 0.0131 \mu\text{m}$. This is equivalent to a 0.0093 μm rms figure error ($\lambda/68$ rms at 633 nm) on both telescope mirrors.

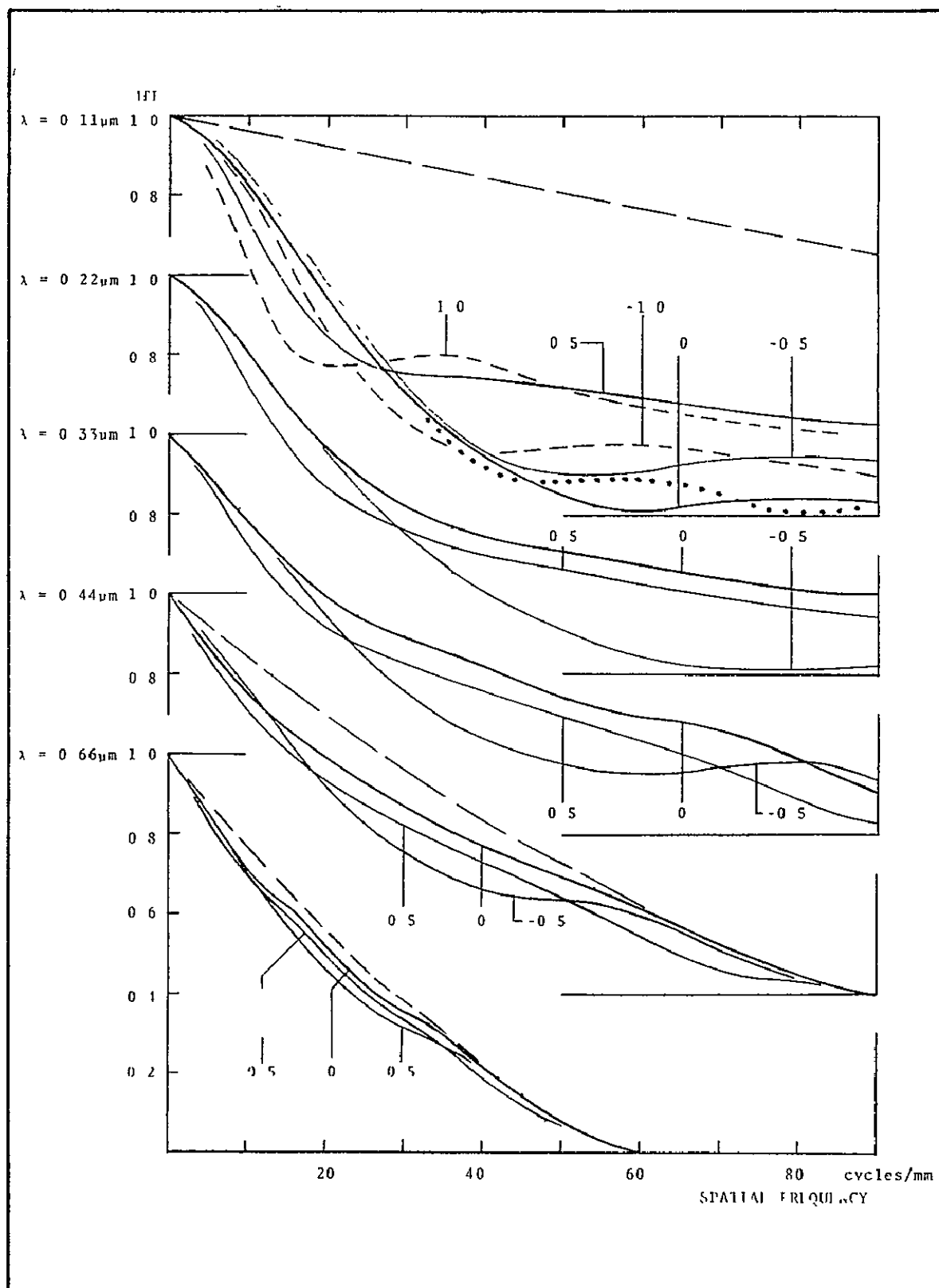


Figure 3-4 Modulation transfer functions for figure profile A (Figure 3-3)

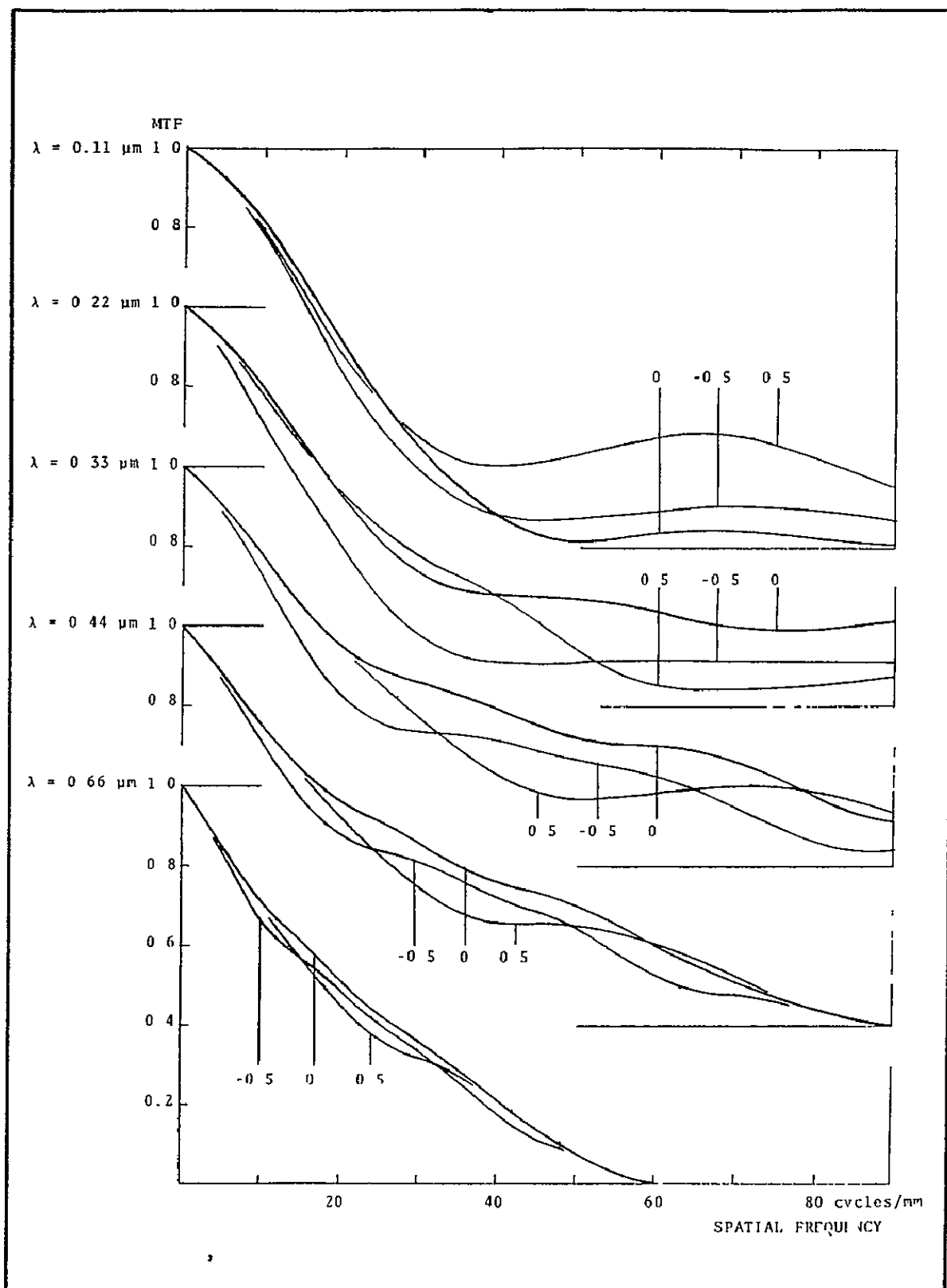


Figure 3-5 Modulation transfer functions for figure profile B (Figure 3-3)



Profile B was constructed under the same conditions as profile A, but is composed of four circle polynomials, i.e.

$$\begin{aligned} R(\rho) &= 0.03[(1/3)R_{10}^0(\rho) - (3/14)R_8^0(\rho) - (5/6)R_6^0(\rho) + (5/7)R_4^0(\rho)] \\ &= 0.03(84\rho^{10} - 225\rho^8 + 200\rho^6 - 60\rho^4 + 1) \mu\text{m} \end{aligned} \quad (3.14)$$

The rms value is $R_{\text{rms}} = 0.0140 \mu\text{m}$, which is equivalent to $0.0099 \mu\text{m}$ rms ($\lambda/64$ rms at 633 nm) on each mirror. The focus shift is 0.036 mm .

MTF in Focussed Telescope. With the above data, diffraction MTFs were calculated at the 5 wavelengths below. These were selected to give round-number cutoff linear spatial frequencies ν_o , as indicated.

λ (μm)	$\nu_o = 2r/(\lambda f)$ (cycles/mm)
0.11023	360
0.22046	180
0.33069	120
0.44092	90
0.66138	60

The results are summarized in Figures 3-4 and 3-5. The curves, marked 0, represent the MTF in the gaussian image plane. In each diagram, the similarity of the curves for the various wavelengths is most conspicuous, especially at low spatial frequencies. Also, there are only minor differences between the curves for profile A and those for profile B. In both cases, the spatial frequency for 50 percent modulation, for instance, varies from 21 cycles/mm at $0.66 \mu\text{m}$ through a weak maximum of 24-28 cycles/mm between $0.44 \mu\text{m}$ and $0.33 \mu\text{m}$ back to 20-22 cycles/mm at $0.11 \mu\text{m}$. The same phenomenon has been observed in other work at BBRC, in which



entirely different error profiles were used, as well as in MTFs calculated for the LSO at Itek, which were based on the topography of an actual mirror (Ref. 3.6). Presumably, as the wavelength decreases from $0.66\text{ }\mu\text{m}$ to $0.11\text{ }\mu\text{m}$, the limitation by diffraction is gradually taken over by wavefront aberrations, thus rendering the low frequency part of the MTF almost independent of wavelength.

At high spatial frequencies, the change in MTF with wavelength is of an entirely different character than at low frequencies. For wavelengths above $0.3\text{ }\mu\text{m}$, the high frequency response stays very close to that of a perfect telescope with obscuration 0.12, as shown by broken lines for $0.66\text{ }\mu\text{m}$ and $0.44\text{ }\mu\text{m}$ in Figure 3-4. However, below $0.3\text{ }\mu\text{m}$, the MTF rapidly falls below the perfect telescope values. This is demonstrated by the wavelength dependence of the frequencies for 10 percent modulation (Rayleigh criterion) listed below.

Wavelength (μm)	Spatial Frequency for 10% Modulation (cycles/mm)		
	Model A	Model B	Perfect Mirrors
0.66	48	48	48.6
0.44	70	71	72.9
0.33	91	93	97.2
0.22	130	125	145.8
0.11	45	38	291.5

For very small wavelengths, the diffraction MTF approaches the "geometrical" MTF, i.e., the convolution of the geometrical ray-height distribution with a sinusoidal object. For profile A, this is shown by the dotted line for $\lambda = 0.11\text{ }\mu\text{m}$ in Figure 3-4.



Although it is hardly justified to base general conclusions on only two models, the above indicates that, in the presence of figure errors of about $0.010 \mu\text{m}$ per mirror (total wavefront error $0.028 \mu\text{m}$ rms), the angular resolution capability reaches a maximum in the near UV and that the resolution at this maximum could still be as high as $0.1''$ (spatial frequency 66 cycles/mm) or better, as measured by the Rayleigh criterion.

MTF in Defocussed Telescope. The MTFs at focus positions $\Delta f = +0.5 \text{ mm}$ and $\Delta f = -0.5 \text{ mm}$ were also calculated. The corresponding curves in Figures 3-4 and 3-5 are labeled +0.5 and -0.5, respectively.

As might be expected, the defocus effect at $0.66 \mu\text{m}$ is rather small, but deviates noticeably from that in a perfect telescope. In particular, there is a marked difference between the MTFs for opposite defocus. The reason is that the ρ^2 wavefront deviation, associated with defocussing (Eq. 3.2) must be added to or subtracted from the wavefront deviation given by Eq. (3.10) or (3.14), depending on the sign of Δf . Only in a perfect telescope is the defocussing effect exactly symmetrical (see, for instance, Ref. 3.7).

As the wavelength decreases, the relative magnitude of the defocus effect increases. The largest deviations occur at the middle frequencies for the wavelength in question, but shift to higher frequencies on an absolute scale. As a result, the modulation loss at low spatial frequencies ($\nu < 30 \text{ cycles/mm}$, resolution less than $0.2''$) depends only weakly on wavelength. However, at higher spatial frequencies, the defocus effect becomes progressively more dependent on the figure-error profile and the sign of Δf . This is evident, in particular, at $\lambda = 0.11 \mu\text{m}$, where



the MTF above 60 cycles/mm is actually better at both $\Delta f = +0.5$ mm and $\Delta f = -0.5$ mm than at $\Delta f = 0$. The explanation is that the geometrical-optical image ($\lambda = 0$) consists of distinct concentric rings, which are formed by the various zones in the mirror profile and consecutively come to focus as Δf is changed. For instance, the wide zone between $\rho = 0.4$ and $\rho = 0.6$ in profile A (Figure 3-3) forms a ring of about 20 μm (0.13") diameter in the gaussian image plane, which focusses at $\Delta f \approx 1$ mm. The corresponding MTF is shown in Figure 3-4 by a broken line. A similar focus is formed at $\Delta f \approx -0.7$ mm by the zone at $\rho = 0.85$. Clearly, this is an artifact of the concentric figure-error models used here. The corresponding phenomenon in actual telescopes is that the image forms an irregular blur, which changes shape in a large range of focus settings without showing a distinct minimum.

Insofar as justified by the particular choice of models used here, the general conclusions that can be drawn from the above are:

1. For all wavelengths, a focus error of 0.5 mm at the gregorian focus (10 μm despace) does not seriously impair the MTF characteristics above 25 cycles/mm (modulation $\approx 50\%$ at a resolution of 0.25").
2. For wavelengths above 0.3 μm , a resolution of 0.1" (Rayleigh criterion) is possible within a focal range of ± 0.5 mm.
3. For far-UV wavelengths, the defocus effect is virtually unpredictable and cannot serve as a basis for the establishment of a focal tolerance.



4.0 THERMAL EFFECTS ON ALIGNMENT

This section describes the effects of periodic insolation of the SOT on the spacing and centering of the telescope mirrors in the thermal environment provided by the LPS and concludes that focus and centering updates may be necessary at intervals of 5 min and 30 min, respectively. This is based on the assumption that the truss material is aluminum. An athermal structure (graphite - epoxy, for instance) is not considered.

4.1 THERMAL ENVIRONMENT OF TRUSS STRUCTURE

The thermal control concept developed in the LPS study is based on the following principles.

1. The entire LPS ensemble is enveloped in a thermal shroud that is stabilized to $10 \pm 3^{\circ}\text{C}$. The upper and lower limits refer to the mean local temperature in different parts of the shroud in various orientations of the LPS with respect to the sun, the earth and the Shuttle. In a particular, fixed orientation, the local variations may be much smaller, say less than 1°C .
2. The mean temperature of the primary mirror is held close to the fabrication and test temperature of 21°C by radiative heaters. During solar observations, the heating is reduced. The absorbed solar energy and the heating surplus are dissipated to space through the LPS shroud, with minimum thermal interaction with the truss structure.
3. The three heat-rejection mirrors (heat-shield ring at the primary mirror, prime-focus heat-rejection mirror and folding mirror) are, likewise, heat-sunk to the LPS shroud and isolated from truss structure as well as possible.



4. The front of the LPS ensemble is shielded by a front plate, which again is heat-sunk to the shroud.
5. The longerons and other truss elements are all enveloped in multi-layer insulation (MLI). The truss structure floats thermally in the environment provided by the LPS shroud, the solar facilities, and the telescope elements inside the truss.

The above approach offers the best stability that can be achieved by passive means in the thermally sensitive aluminum truss structure. The remaining temperature variations are small and can be predicted only by detailed modeling of all internal LPS subsystems, for which sufficient definition is not available at this time. Detailed thermal analysis is required for the definition phase of the SOT concept. This is demonstrated by the fact that a uniform temperature increase of only 0.04°C is sufficient to change the mirror separation by $5\text{ }\mu\text{m}$. This is the tolerance accepted in this study as a design goal.

For the present study, we will restrict ourselves to an estimate of the thermal response of the truss in one particular case only, namely, alternating solar and stellar observations. This represents the most intensive use of the SOT and is, undoubtedly, the most severe systematic thermal load cycle to which the truss can be subjected.

4.2 TRUSS RESPONSE TO INTERMITTENT INSOLATION

The front aperture has a diameter of 134 cm. The power entering the SOT amounts to about 2000 W. The distribution of the incident energy over the SOT optical components is listed in Table 4-1. For the primary mirror, we assume 85% integrated spectral reflectivity, 14% absorption and 1% scattering. For the heat-rejection

Table 4-1
ESTIMATED DISSIPATION OF RADIATIVE ENERGY IN TRUSS STRUCTURE

	Diameter (cm)	Incident power* (W)	Absorbed, scattered (W)	Dissipated in truss (W)
Front cover	≈400	≈18000	2700	3
Front aperture	134	2016	--	-
Primary mirror	125	1670	250	4
Secondary mirror pod	25	92	28	1
Heat-rejection ring (primary)		254	33	1
Heat-rejection mirror (focus)		1420	185	3
Heat-rejection folding mirror		1235	161	3
Total dissipated in truss (W)				<u>15</u>

*Based on incident flux of 0.144 W/cm^2 (earth at perihelion)



mirrors, the numbers are 87%, 12% and 1%. Structural elements, exposed to the sun, are assumed to be gold-plated, with an integrated absorptivity of 30%.

To estimate the heating of the truss structure, we consider each of the elements in Table 4-1 separately:

1. The primary mirror is controlled to maintain a constant mean temperature. The variation in input into the truss structure is, therefore, a second order effect, which could not amount to more than a few watts.
2. The heat-rejection mirrors quickly rise to an elevated temperature and dissipate heat by radiation. We assume that the fraction intercepted by the truss is the ratio of its projected area relative to that of the shroud (21%) and that the structure is covered by MLI with an outer layer of black polyimide to minimize light scattering. This transmits an estimated 7% of the incident radiation to the structural elements underneath.
3. The LPS front cover radiates only a small fraction of its heat content into the cavity, formed by the telescope. Its effect on the truss is almost negligible, provided conductive heating can be effectively suppressed.
4. For the secondary-mirror pod, both heating by direct insolation and by radiation from the heat rejection mirror are of concern. The support structure is movable and must be accurately indexed to the truss structure, making heat conduction almost unavoidable. Even a small heat flow can create significant temperature gradients in the vicinity of the prime focus, both in the secondary mirror structure



itself and in the truss longerons. To alleviate these problems, separate mounting of the heat-rejection mirror, athermal construction of the pod and shielding from direct illumination by the sun should be considered.

The total power, dissipated into the truss by the above effects (counting radiative coupling only), is of the order of 15 W. We first make the extremely simple assumption that this input is distributed uniformly through the structure. It then follows that the temperature in each of the longerons (ignoring the remainder of the structure) increases at a rate of 0.12°C/h (see calculations in Table 4-2). This uniform heating causes a despace error only and would suggest minimum update intervals of 20 min.

The above number applies to the initial heating at first exposure to the sun only. If, after 1 hour, for instance, the SOT is pointed at a star, the temperature decreases, but is still higher than the initial temperature when, 30 min later, solar observations are resumed.

If the observation cycle is repeated, the mean truss temperature will gradually increase until a steady-state level has been reached. The better the truss insulation, the higher the steady-state temperature will be and the greater the number of orbits to reach this state. In Figure 4-1, the temperature changes at the onset of the solar and stellar observations are shown as a function of the heat-loss time constant τ of the truss. In all cases, the input power is assumed to be the same, i.e., 15 W. This assumption is not quite justified, since the input is likely to be greater if the insulation is less. This would indicate that a large time constant is desirable to minimize the steady-state temperature fluctuation, but at present it is not possible to predict what time constant could be realized technically.

Table 4-2
THERMAL RESPONSE OF TRUSS

Length longerons	700 cm
Diameter	45 cm
Wall thickness	0.6 cm
Density aluminum	2.7
Mass	$1.6 \times 10^5 \text{ g}$
Specific heat aluminum	$0.22 \text{ cal g}^{-1} \text{ } ^\circ\text{C}^{-1}$
Heat capacity, 3 longerons	$1.1 \times 10^5 \text{ cal } ^\circ\text{C}^{-1}$
Heat input	$15 \text{ W} = 3.6 \text{ cal sec}^{-1}$
Temperature rise rate	0.12 cal h^{-1}

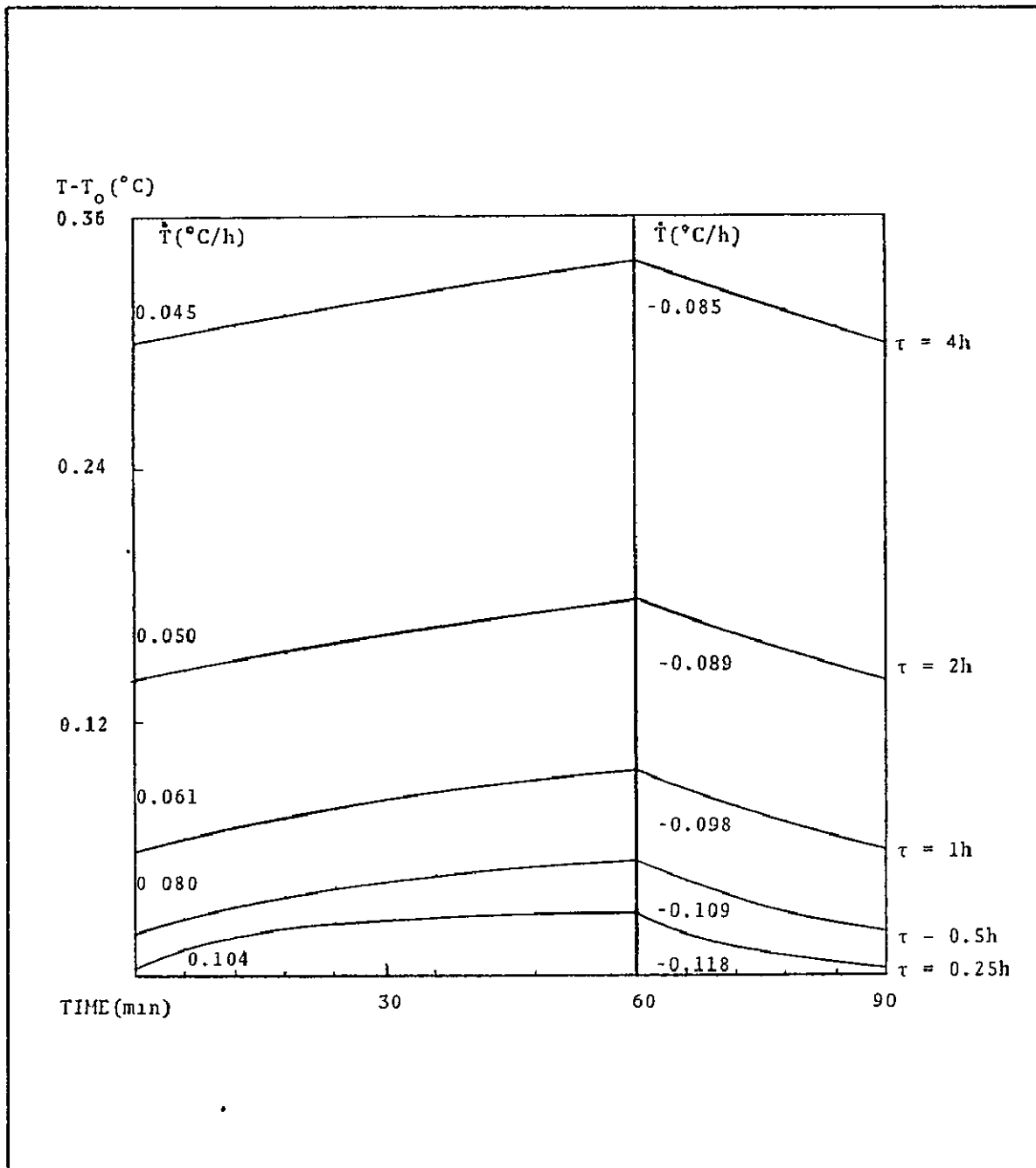


Figure 4-1 Steady-state temperature fluctuations in truss for uniformly distributed input of 15W during 60 min exposure to sun, followed by 30 min exposure to space, for various truss time constants τ . T_0 is the LPS shroud heat-sink temperature. The initial temperature change T is smaller for larger τ .



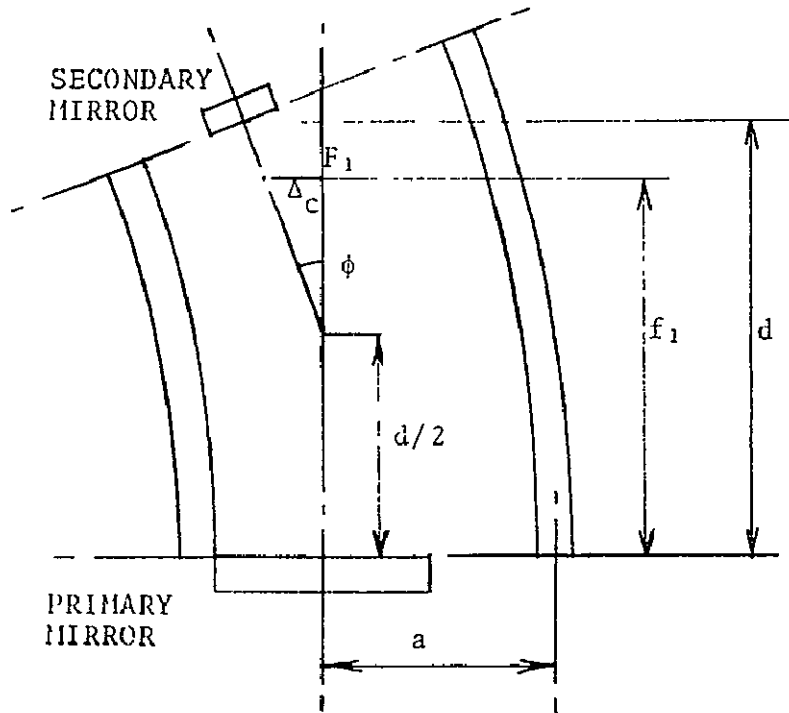
Since the three longerons are coupled by cross members with relatively high thermal resistance and are shielded effectively against radiative heat exchange, it is likely that their mean temperatures build up differently. The result is bending of the truss, which introduces lateral separation of the prime focus and the secondary-mirror first conjugate (decentering). We consider the particular case of two longerons at a temperature $T_0 - \Delta T/2$ and one longeron at a temperature $T_0 + \Delta T$. The corresponding decentering error is

$$\Delta_c = (1/2)(1 - \gamma^2)(f_1^2/a)\alpha \Delta T,$$

where γ is the central height ratio, f_1 the primary focal length (Table 1-1), a the distance of the longeron to the telescope axis (Figure 4-2), and α the thermal expansion coefficient of aluminum ($\alpha = 25 \times 10^{-6}$). From this it follows that for $\Delta T = 0.3^\circ\text{C}$, $\Delta_c = 75 \mu\text{m}$, which is the decenter tolerance, assumed for this study. Temperature differences of this magnitude are unlikely to occur in the first few observation cycles, but could conceivably build up in the steady-state if the truss time constant is very large. However, it would seem that this build-up could easily be handled with a decenter correction once per orbit or prior to each solar or stellar observation period. At the same time, the above indicates that too large a time constant might become detrimental to centering stability, which should be given consideration in the selection of this constant.

4.3 RECOMMENDED FOCUS AND CENTERING UPDATE INTERVALS

The above derivation of the update intervals is based on radiative heating of the truss only. As pointed out in the discussion of the heat inputs from the secondary mirror pod, sizable contributions may arise from conductive heating. Also, the interaction with the solar facilities and the shroud may occasionally introduce



$$\Delta_c = (f_1 - d/2) \phi$$

$$\phi = \alpha (d/a) \Delta T$$

$$d = (1 - \gamma) f_1$$

$$\Delta_c = (1/2) (1 - \gamma^2) (f_1^2/a) \alpha \Delta T$$

Figure 4-2 Decentering Δ_c caused by bending of truss



noticeable temperature changes. These effects may cause significant temperature gradients if the heating of the longerons is not uniform, as is very likely, considering the localized character of the heat sources.

For lack of a quantitative assessment of these effects, we must allow for a considerable safety margin. For this reason, we base the alignment concepts in this study on the following minimum update intervals:

- Focus: 5 minutes
- Centering: 30 minutes

This assumes that detection and correction within a small fraction of the tolerance is possible. If the control accuracy is comparable to the tolerance, continuous control is necessary (e.g., every few seconds), regardless of thermal stability.

The general conclusion from this section is that an aluminum structure would indeed seem acceptable for the SOT. However, future mechanical and thermal designs must go hand-in-hand to assure that local thermal inputs remain small and that a sufficiently large time constant for the structure is achieved. Absolute control within fractions of a centigrade is not necessary, as long as changes are gradual, both in location and in time.



5.0 ALIGNMENT SENSING

This section describes the principles and the basic optical instrumentation needed for detection of focus and centering errors. The full gregorian telescope and the prime-focus mode of operation are treated separately. Only in the first case does the alignment precision have to be commensurate with the full telescope resolution capability.

For focus sensing at the gregorian focus, this study compares a geometrical-optical method with an interferometric method. The former is based on detection of the point of intersection of two marginal rays (i.e., rays passing through opposite points at the edge of the telescope entrance stop) from an auxiliary light source. This method is relatively simple, but offers only limited accuracy. The interferometric method is much more complicated, but provides a detection accuracy of $1/5$ of the focal tolerance, or better. This has the very significant advantage that the major portion of the tolerance is left for drift between settings, without active control.

For detection of centering errors in the full gregorian telescope, a geometrical-optical method suffices. This is implemented by two reimaging projectors, mounted at the rim of the primary mirror, which sense lateral displacements of the secondary by reflections from small spherical mirrors mounted at its periphery. The sensor output also provides coarse despace information, which is convenient for initial alignment on orbit and for bringing focus within the inherently small range of the precision sensor at the gregorian focus.

In the prime-focus mode, focus and centering errors are detected simultaneously by position sensors on the prime-focus instrument, which are illuminated by the two projectors mentioned above. Each prime focus instrument has its own set of sensors, to compensate



for any alignment errors, introduced by the instrument exchange mechanism.

5.1 FOCUS SENSING AT GREGORIAN FOCUS

The gregorian focus position is affected by changes in the mirror separation d , the primary focal length f_1 , the secondary focal length f_2 , as well as the structure defining the image distance, q .

The baselined approach to focus control in this study is the following:

- The compound effect of all focus-error contributions is measured with respect to a reference plane near the gregorian focus.
- The scientific instruments are indexed to this reference plane.
- Focus corrections are made exclusively by adjustment of the mirror separation, d .

In the above approach, thermal changes in the dioptric power of the mirrors and in the optical train between the secondary mirror and the reference plane are not corrected separately, but compensated by a commensurate change in d . This procedure introduces some departure from the nominal telescope parameters, but these are so small that the image quality is not noticeably affected.

In order to use the same mechanism for focus control in the gregorian and the prime-focus modes of operation, the adjustment of d is implemented by an axial displacement of the primary mirror.

Internal focus changes in the scientific instruments are not compensated by the above method. These must be considered separately as part of the instrument design and instrument-telescope interface.

5.1.1 Candidate Focus-Sensing Methods

The most direct way to sense focus position would be in the telescope image itself. For the sun, this could conceivably be done by analysis of the spatial frequency content in the image. This could be combined with image-motion sensing for IMC. The latter



is presently under study elsewhere, but results are not available at present. For stars, a different technique would have to be used, such as visual judgment of a televised image by the Payload Specialist. However, considering the wide variety of objects to be studied by the SOT, it is much more attractive to use a focus-sensing method that is independent of the characteristics of the object under observation. Two approaches suggest themselves. One is to determine the point of intersection of two marginal rays, and the other is to measure the variation of the optical path difference across the pupil. An example of each is discussed below. These examples were selected to meet the following prerequisites:

1. The sensing beams are fully separated from the telescope beam at the entrance pupil, but pass entirely through the field stop at the prime focus.
2. The sensing optics do not affect the heat-rejecting system.
3. The light source is a laser diode or a light-emitting diode (LED), with a wavelength of 905 nm, which is pulsed to minimize mutual interference with solar observations if active focus control during observations is necessary. Narrow-band filters at the detectors reject most of the solar radiation.

In both cases, the sensing method is immune to tilt of the primary mirror around the prime focus, while the effects of decentering of the primary and tilt of the folding mirrors can readily be eliminated.

5.1.2 Geometrical-Optical Method

Principle. Two narrow beams from a small source in the vicinity of the telescope focus traverse the telescope in opposite directions, as shown in Figure 5-1. Two images are formed, the

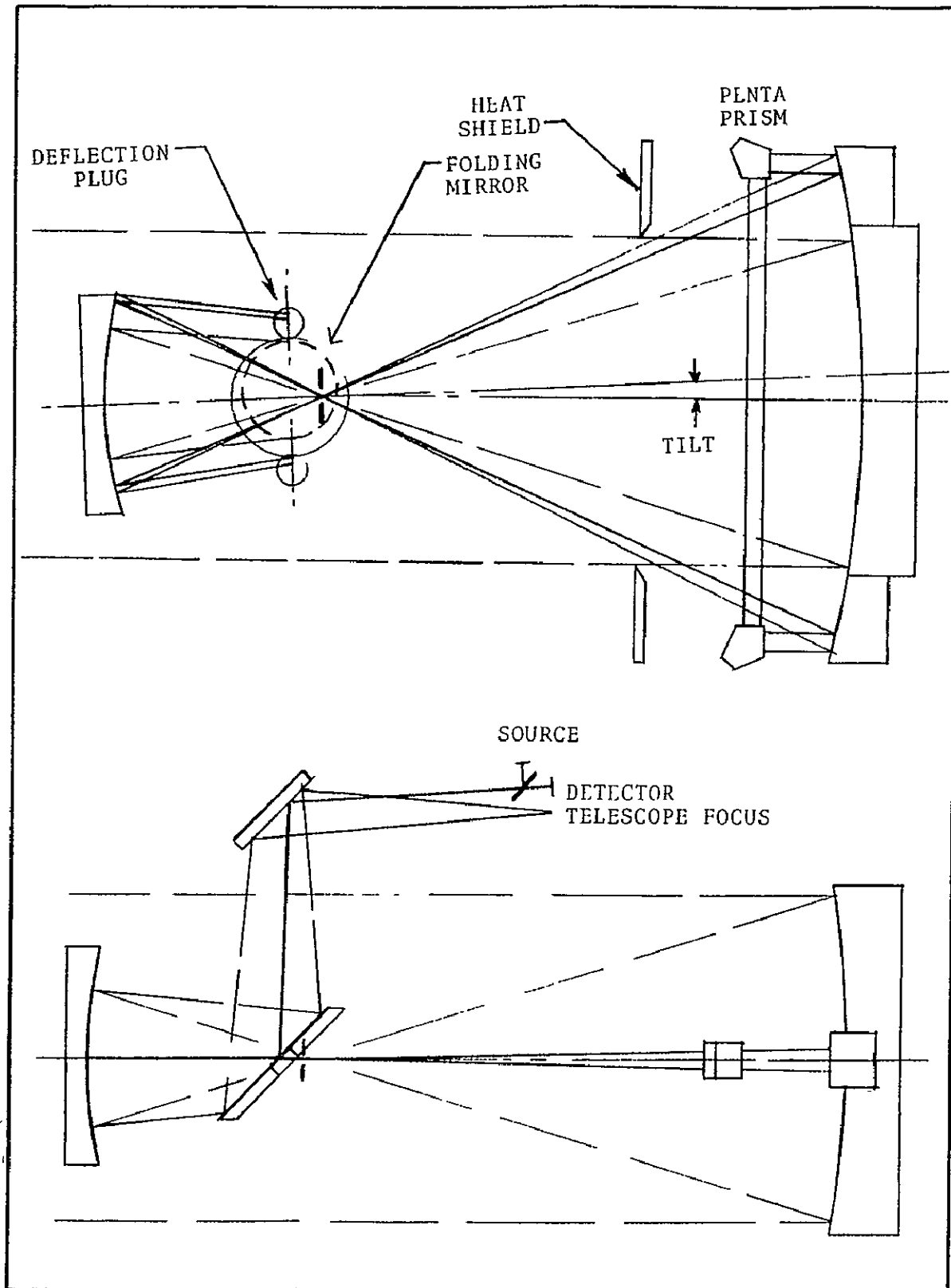


Figure 5-1 Geometrical-optical focus sensing at gregorian focus



position of which is determined with a silicon quadrant photocell. This method has been proposed by Perkin-Elmer for the LSO (Ref. 5.1) and is a variant of a device described by Strong (Ref. 5.2) to monitor collimation. A similar method is used for co-alignment of the Smithsonian/University of Arizona multiple-mirror telescope (Ref. 5.3). The source and the detector can be separated by means of a beamsplitter (as shown) or by a small folding mirror. The illuminator/detector assembly is separated from the telescope field by deflecting the beams off small tilted inserts in one of the folding mirrors, preferably the first one, which lies close to the telescope exit pupil. Auxiliary mirrors are cemented to the rim of the primary mirror to extend the parabolic surface. However, spherical mirrors, conforming to the local curvature, are adequate. The secondary mirror is unmodified, but must be enlarged at the expense of some obscuration to accommodate the beams.

Optics. The focus-sensing beams are strung through the telescope in such a manner that the inserts at the folding mirror completely clear the telescope beam for all primary mirror tilts τ . If the pentaprisms and the heat shield are attached to the primary mirror, as shown in Figure 5-1, the inserts must be large enough to allow for $\tau = \pm 9.46$ mrad. This is the tilt needed to point the SOT to one solar radius beyond the limb, while the LPS is pointed at the center of the sun. The above condition for clearance is

$$r - \tau f_1 < h_m + \tau f_1 - r_p \quad (5.0)$$

where h_m is the height of the center of the focus-sensing beam at the primary mirror and r_p the beam radius. The left side of Eq. (5.0) is the telescope beam height at the primary, relative to the telescope axis, the right side is the minimum height of the edge of the focus-sensing beam. Some numerical examples are ($r = 625$ mm):



r_p	20	30	40
h_m , minimum (mm)	730	740	750
$h_m + r_p$, minimum (mm)	750	770	790

A large beam diameter is desirable to keep the size of the diffraction image at the detector small. However, this requires large pentaprisms and complicates accommodation of the auxiliary mirrors (maximum height $h_m + r_p$), as will be discussed in Section 5.4.

For this study, we will assume $r_p = 30$ mm and leave further trades to future developments.

The above beam diameter ($2r_p$) refers to the return beam. Stops are placed on or near the pentaprisms. The incident beam has a diameter equal to $2r_p - 2\tau f_1$, to allow for all mirror tilts. The incident beam fully fills the inserts at the folding mirror and is defined by aperture stops in the illuminator.

The illuminator is shown in Figure 5-2. The light-source is imaged on the field stop, which is acceptable, since the image at the detector is spread out by diffraction. Alternate imaging of the source on the aperture stops may be considered in detailed developments.

An alternate to the configuration shown in Figure 5-1 is to keep the pentaprisms fixed. The inserts in the folding mirror can then be considerably smaller, but the prism size roughly triples. This option is not further considered here.

Accuracy. The minimum detectable focus error is estimated as follows: A beam diameter $2r_p$ at the primary mirror produces a diffraction image with an equivalent diameter

$$2a = (2/\pi)\lambda f/r_p \quad (5.1)$$

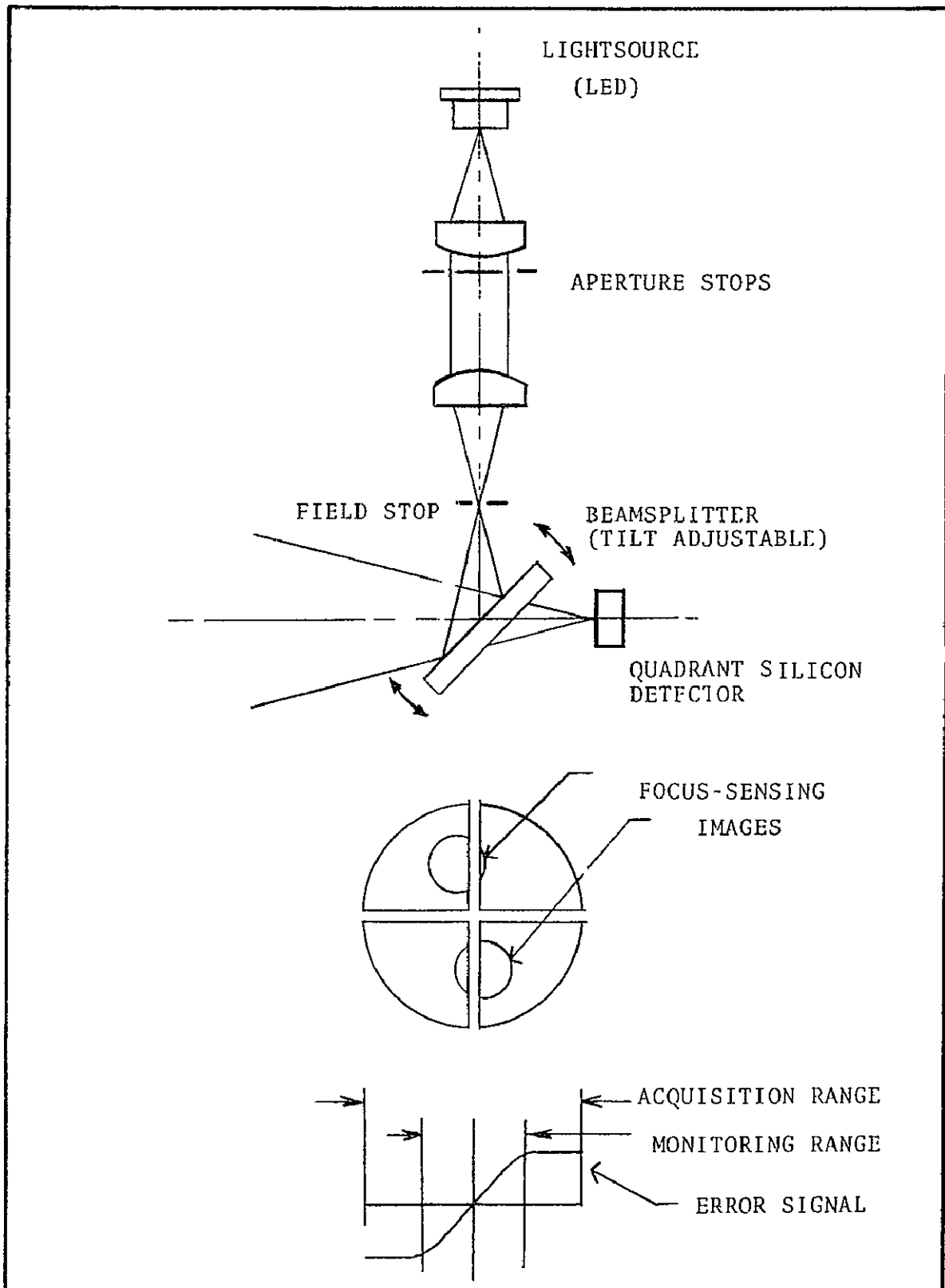


Figure 5-2 Focus-sensing illuminator and detector



For $\lambda = 905 \text{ nm}$, $f = 31,500 \text{ nm}$ and $r_p = 30 \text{ nm}$, we find $2a = 1.2 \text{ mm}$. We assume now that the center of the image can be detected within 1% rms of the effective diameter. This requires a minimum detectable photometric unbalance between the silicon detector quadrants of 2.5% rms (Figure 5-2). This leads to a position-detection accuracy of $12 \text{ } \mu\text{m}$ rms in each beam and to an accuracy of $12\sqrt{2} = 17 \text{ } \mu\text{m}$ rms in their difference. This corresponds to a focus detection accuracy of 0.43 mm rms for a single pass through the telescope and a 0.22 mm rms for a double pass. This is practically equal to the focal tolerance, assumed as a goal for this study and only half of the target tolerance considered acceptable. This means that continuous active focus control would be necessary, since no margin is left for uncontrolled drift. However, in actual laboratory measurements at BBRC, a nulling accuracy of $3 \text{ } \mu\text{m}$ rms has been reached with silicon quadrant sensors of this size (Section 5.2). This suggests that the above estimate of the achievable accuracy may be overly conservative and that the ultimate detector limit of the geometrical-optical method is actually of the order of $1/4$ of the 0.25 mm focal tolerance. This would leave a reasonable margin for drift without active control. Further detailed study of the achievable detection limit is clearly indicated and should include a wide search of applicable detectors.

Tilt and Decenter Effects. Accurate focus sensing requires that both images straddle the dividing line between the quadrants. This places an upper limit on the permitted decentering of the primary mirror and on additional tilts in the optical train following the secondary mirror. For the above value of a , the tilt-induced image shift should not be more than 0.35 mm , for instance, which corresponds to $50 \text{ } \mu\text{m}$ at the prime focus. This suggests that centering should precede focusing, which is the most logical procedure anyway, because the centering system is needed already to provide coarse "prefocussing" (Section 5.2).



For fully unperturbed focus sensing, one could consider to use the summed signals of the focus sensor for tilt correction by rotation of the beam splitter, for instance. This would almost become mandatory if the focus-sensing accuracy were improved by use of a smaller wavelength (e.g., 600 nm) or a larger beam diameter.

Range. The monotonic range of detection is approximately equal to the image diameter. Within this range, the focus position can be read out unambiguously, which is convenient, e.g., for manual adjustment after reacquisition. The full acquisition range (saturated error signal) is determined by the diameter of the detector. Sufficient overlap with the centering-error detection system can already be reached with a detector of 2.5 mm diameter.

5.1.3 Interferometric Method

Optical Path Difference. The interferometric method is based on the fact that a focus error Δf introduces an optical path difference between the central ray and a marginal ray (height h) equal to

$$s = (1/2)\Delta f(h/f)^2 \quad (5.2)$$

Optical path differences can be measured interferometrically to an accuracy of 0.01λ , or better, without much difficulty. For $\lambda = 905 \text{ nm}$, this amounts to $0.009 \mu\text{m}$ in s , or $46 \mu\text{m}$ in Δf , i.e., $\approx 1/5$ of the focal tolerance. If the telescope is passed twice, a detection accuracy of $23 \mu\text{m}$ is easily reached. This is less than $1/10$ of the tolerance. For this reason, serious consideration should be given to an interferometric method for focus-error detection at the gregorian focus, even though the implementation is more complex and the detection range rather limited, as will be discussed in the next sections.

ORIGINAL PAGE IS
OF POOR QUALITY



Three-Beam Interferometry. For this study, we consider a focus-sensing system based on a method devised originally by Vaisala (Ref. 5.4) and applied later by Zernike (Ref. 5.5) to the measurement of small optical retardations. This method is the following: In the vicinity of the telescope focus, two marginal beams from an auxiliary source produce nearly flat wavefronts, which intersect at an angle 2 r/f (Figure 5-3A). These form common two-beam sinusoidal interference fringes. The amplitude distribution in the plane, bisecting the wavefronts, is shown in Figure 5-3B. The wavefront from a central beam from the same source is superimposed upon this distribution. In perfect focus, this results in enhancement of the even fringes, and suppression of the odd fringes (Figure 5-3C). If a focus shift is introduced, which causes a $\lambda/2$ retardation of the central beam, the reverse occurs (Figure 5-3D). However, if the focus shift produces a $\lambda/4$ path difference, the composite amplitude in all fringes is the same and the even and odd fringes appear equally bright (Figure 5-3E). Focus-error detection is now based on the phenomenon that a small departure $\delta\lambda$ from the $\lambda/4$ position produces a relative brightness difference 2δ between the even and odd fringes, which can be detected photometrically to produce error signals for focus correction (phase diagram, Figure 5-3F). Hence, a 2% rms photometric accuracy provides path-difference detection to 0.01λ rms, which gives the method its high focus-error detection sensitivity.

Implementation. The optical train is shown schematically in Figure 5-4. The source and detector are located in the vicinity of the gregorian focus. The three beams are reflected towards the secondary mirror by way of the telescope folding mirrors and are then directed through the telescope field stop to the primary mirror by three inserts in the secondary mirror. The return path is identical. The reflectors at the primary mirror are spherical

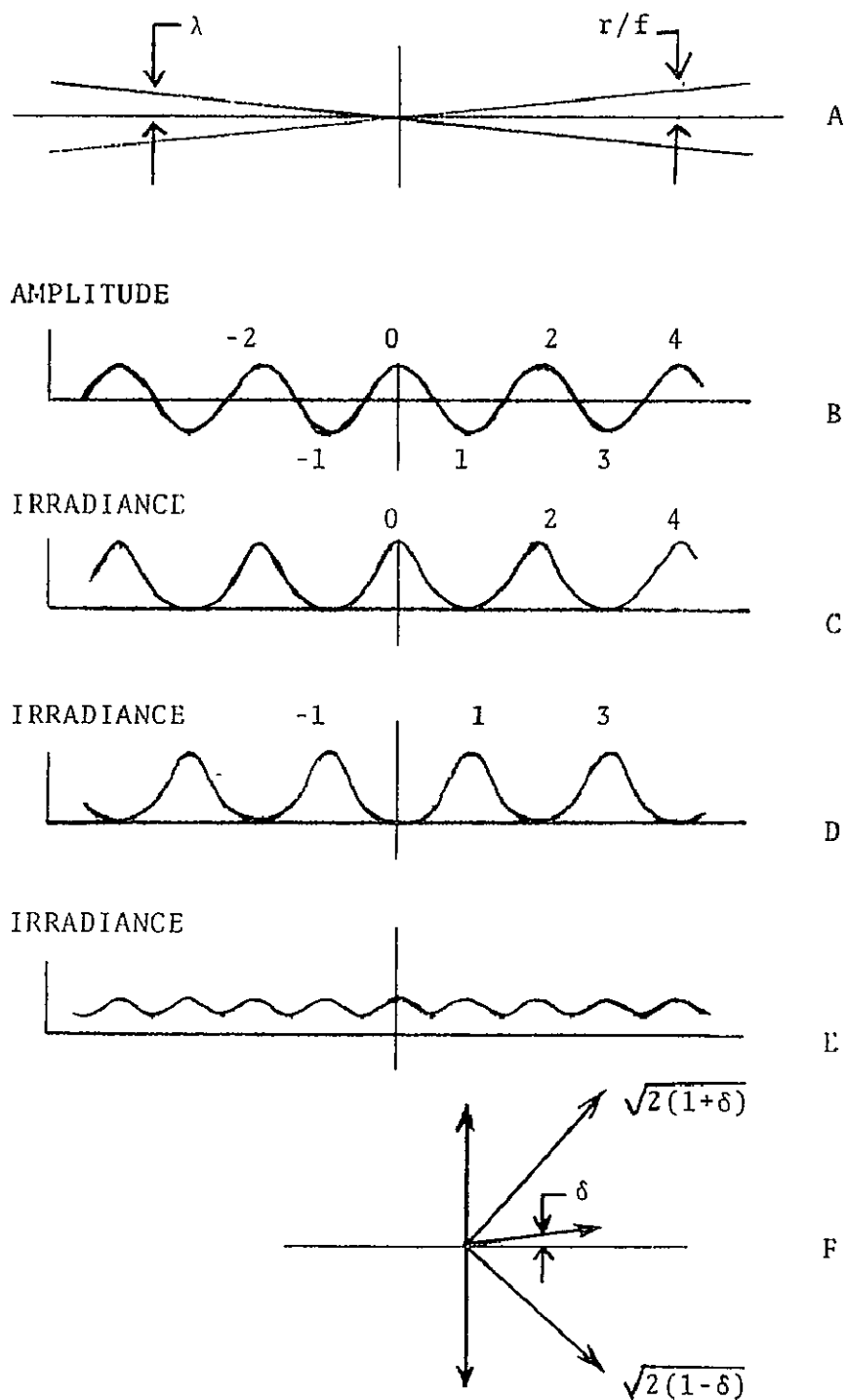


Figure 5-3 Three-beam interferences

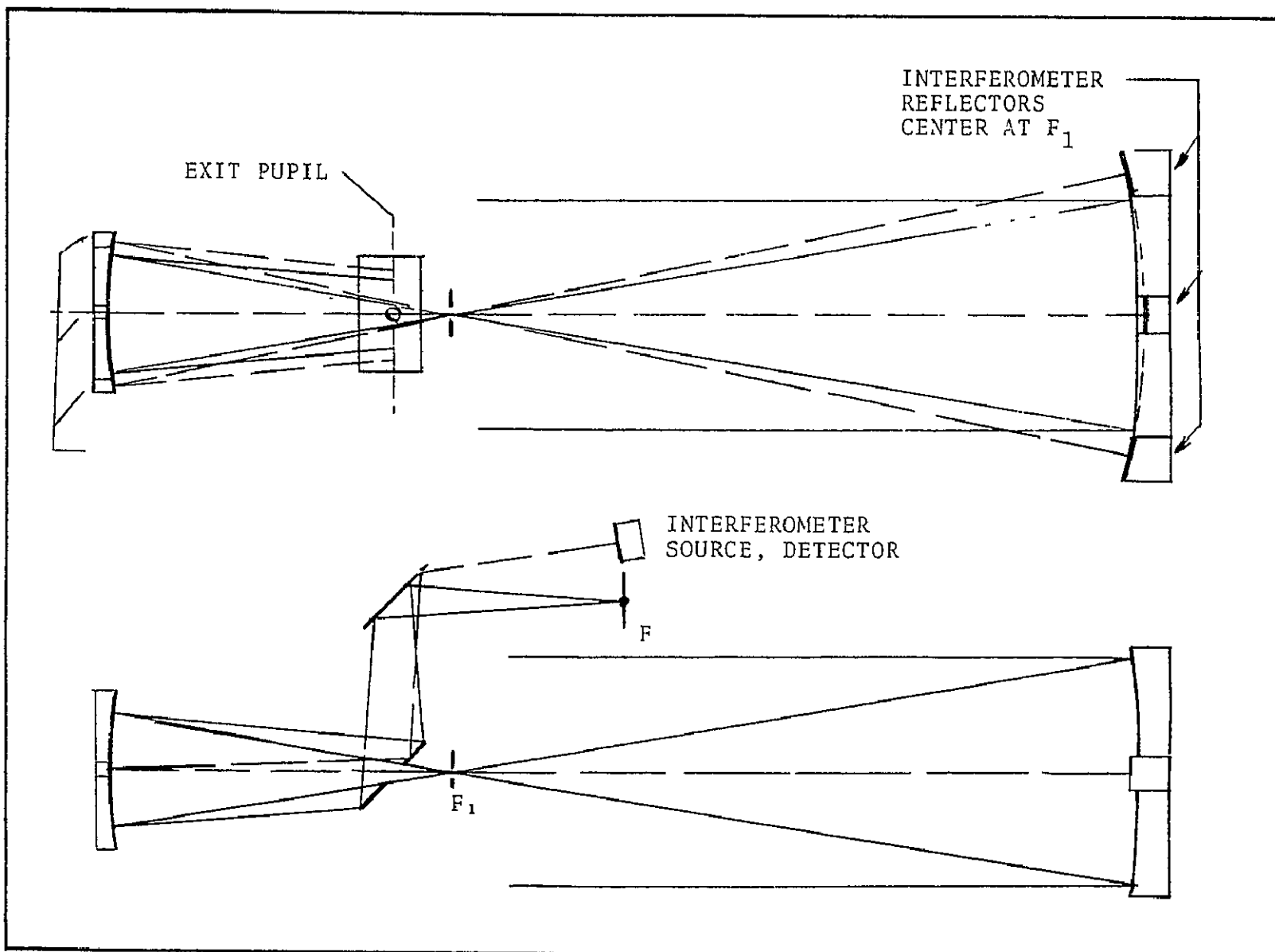


Figure 5-4 Interferometric focus sensing





with their centers of curvature at the prime focus. The reflectors for the marginal beams are cemented to the rim of the primary. The central reflector is either cemented on the mirror or ground directly into the blank.

Interferometer Optics. In principle, the three beams could be defined by aperture stops placed on the primary mirror. However, to illuminate these at all mirror tilts, the incident beams must be oversized and may scatter into the telescope field. The alternate place for stops, the first folding mirror, is excluded because of its central hole. Hence, it is necessary to define the beams by circular aperture stops in the illuminator, similar to Figure 5-2. The projected diameter on the primary mirror may be of the order of 40 to 80 mm for the central beam and half that for the marginal beams. The actual value is a matter of detailed design (see Section 5.4).

The field stop (slit) must be narrow enough not to blur the interference fringes. The spacing of the fringes is equal to $\lambda f / (2h)$, which is about 23 μm (Figure 5-3). Hence, the slitwidth should not be more than about 6 μm . However, the height can be extended to a few cm, to preserve sufficient area.

The returned image can be isolated by a folding mirror (as shown) or by a beamsplitter. Some magnification may be needed to match the rather narrow pattern to the detector. This should be an image-recording device, for which a CCD array is most suitable.

We note that the axial position of the detector should be adjusted to have the $\lambda/4$ position in the focus sensing system correspond to true focus in the telescope. For final calibration on-orbit, readjustment by the Payload Specialist, through remote control, might be considered.



Impact on Central Obscuration. The inserts for the central beam in the telescope mirrors must be kept well within the obscured area, in order to avoid light scattering and local heating by the sun. This necessitates an increase in obscuration, as discussed below.

At the primary mirror, the lower limit for the obscuration ratio β is given by

$$\beta r > a - 2\tau f_1 - d\psi \quad (5.3)$$

where τ is the tilt angle of the primary and ψ the angular radius of the sun. The maximum value is $\psi = 4.73$ mrad (earth at perihelion). This relation is based on the assumption that the LPS is always pointed at the center of the sun during solar observations.

A similar clearance condition exists at the secondary mirror. For a telescope field-of-view 2α , the radius r_c of the free area at the center is

$$r_c = -\gamma\beta r + [(1 - \gamma^2)\alpha - \gamma(1 - \gamma)\tau]f_1 \quad (5.4)$$

This should exceed the interferometer beam radius at the secondary, which is practically equal to $-\gamma a$. This places another limit on β , i.e.,

$$\beta r > a + [(1 - \gamma^2)\alpha - \gamma(1 - \gamma)\tau]f_1/\gamma \quad (5.5)$$

For a field angle $\alpha = 3'$, it is found that the latter condition overrides Eq. (5.3) for all $\tau > 3.7$ mrad.



With regard to τ , we assume the same maximum value as in Section 5.1.2, i.e., $\tau = 9.46$ mrad. This gives the following obscurations as a function of the focus sensing beam diameter $2a$ at the primary mirror:

$2a$ (mm)	20	40	60	80
β (minimum)	0.152	0.168	0.184	0.200

These diameters are all in excess of the obscuration, originally baselined for this study, but neither is detrimental to the telescope image quality.

For marginal beams, the same restrictions apply as in Section 5.1.2. No further discussion is needed here.

Tilt and Decenter Effects, Detection Method. Both tilt of the folding mirrors (image motion compensation) and decentering may displace the interference pattern between focus adjusts. Even stability during refocusing may be a problem. Hence, a detection system is necessary that determines the parity of the fringes from the envelope of the diffraction pattern and subsequently measures the contrast sufficiently fast not to be disturbed by any shifts. The alternative is to stabilize the pattern, as discussed in Section 5.1.2, by control of a folding mirror. In this case, fixed sensors at the even and odd fringes would suffice. Conceivably, this could be done with two masks of parallel slits, one transmitting all even fringes to one half of a split-field silicon photocell and one transmitting the odd fringes to the other half



Range. A distinct disadvantage of the method is that the range of unambiguous detection of focus is very small, namely, not larger than the standard focal tolerance (in double pass) at 905 nm, which corresponds to a path-difference change of $\pm 1/2\lambda$ and a telescope focus change $\Delta f = \pm 1.15$ mm. Stable focus-control positions occur at intervals $\Delta f = 2.3$ mm (path-difference increments λ) (Figure 5-5).

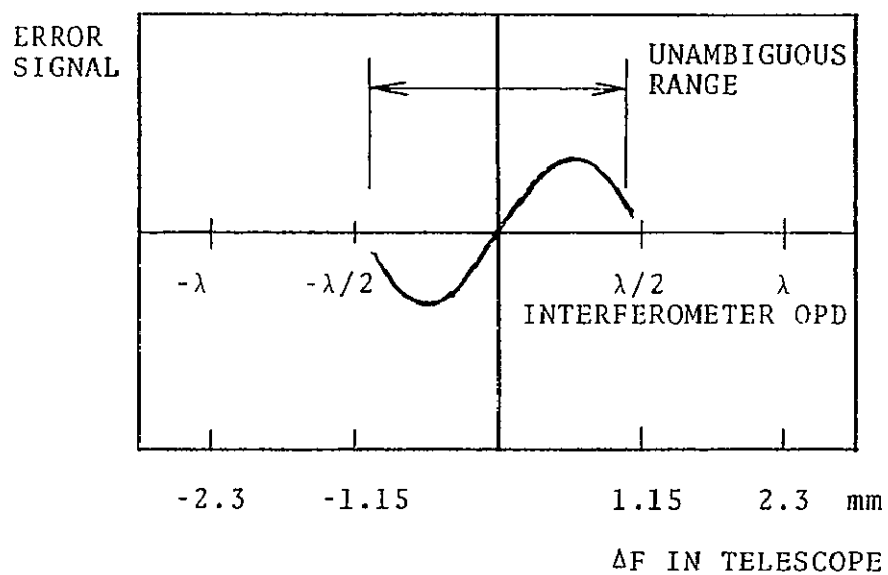
The unambiguous range is hardly larger than the minimum focus error, detectable by the centering-error detection system (Section 5.2). Reliable transfer may not be possible without an intermediate step or by increasing the range at the expense of sensitivity, as will be discussed below.

5.1.4 Comparison of Focus-Sensing Methods

An overview of the accuracies and ranges of the various focus-sensing systems is given in Table 5-1. In addition to geometrical and interferometric sensing at the gregorian focus, the table also lists the prefocus information that can be derived from despace sensing by the centering control system, as will be discussed in detail in Section 5.2.

The geometrical-optical method has the advantages of simplicity and large range, but it may be difficult to reach sufficient accuracy to allow for uncontrolled drift for several minutes. The best way to resolve this question is by experiment in a simulated alignment system.

The interferometric method is complex and requires modification of both the primary and the secondary telescope mirrors. It has ample sensitivity but the range is inadequate. A better balance can be reached if only half the telescope aperture, or less,



ORIGINAL PAGE IS
OF POOR QUALITY

Figure 5-5 Error signal in interferometric
focus sensing

Table 5-1
FOCUS SENSING METHODS FOR GREGORIAN FOCUS

<u>Sensing Method</u>	<u>Prefocus</u>	<u>Geometrical</u>	<u>Interferometric</u>
Accuracy (mm rms)	1.4	0.22 (possibly 0.06)	0.02 or better
Acquisition range (mm)	N.A.	<u>+</u> 30	<u>+</u> 1.2
Monotonic range (mm)	<u>+</u> 3.5	<u>+</u> 0.6	<u>+</u> 0.6
Modifications needed:			
Primary mirror	2 projectors + penta prisms	2 spherical extensions + penta prisms	2 spherical extensions 1 central insert
5-18 Extreme radius * (mm)	\approx 780	\approx 800	\approx 760
Secondary mirror	2 spherical extensions	diameter increase	
Extreme radius *(mm)	\approx 82	\approx 82	\approx 82
Obscuration ratio	0.15	0.15	0.20 **
Folding mirror	-	2 tilted extensions	-

*) Diameter sensing beams at primary mirror 60 mm

**) Obscuration determined by central beam



would be used. Conceivably, this could be done by means of three beams along the edge of the aperture, which would also remove the complications of treading the central beam through the telescope. The viability of the interferometric method in either the full-aperture or partial-aperture version is also best evaluated experimentally.

The effect of thermal deformation of the primary mirror is different in the two methods. The geometrical method maintains focus as defined by the marginal rays. This is not necessarily the best focus, averaged over the entire aperture, because thermal deformation may change the mirror profile. The interferometric method preserves focus only if the mirror expands uniformly. For pure bending, only half the focal change is compensated. In reality, non-uniform edge effects complicate the deformation. These can be assessed only by detailed thermal analysis which is beyond the scope of this study.

5.2 CENTERING SENSING IN GREGORIAN TELESCOPE

Centering concerns only the lateral separation of the prime focus and the first conjugate of the secondary mirror. The tolerance, established in Section 3, is 75 μm . Small fractions of this tolerance can easily be detected by geometrical-optical methods, as will be shown below.

Candidate Centering-Sensing Arrangements. Of the numerous methods that could be conceived, this study recommends the following approach: Two reimaging projectors, aimed at the prime focus, are placed at opposite sides of the primary mirror and detect the position of images returned by spherical reflectors at the edge of the secondary (Figure 5-6). The reasons for this selection are.

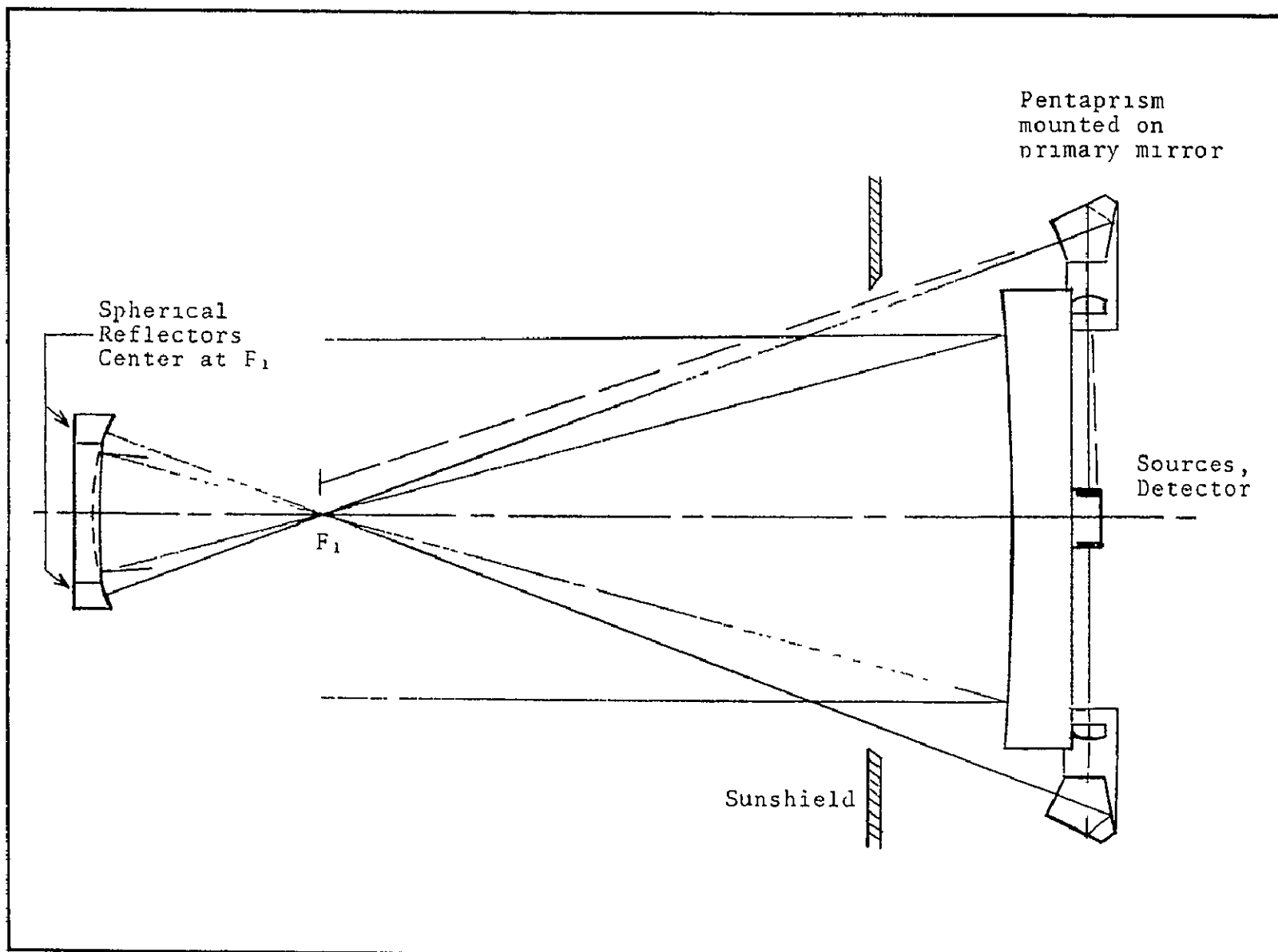


Figure 5-6 Centering sensing



1. The two projectors provide a coarse measurement of mirror separation (despace), which is convenient for initial alignment on-orbit and expands the range of the precision focus-sensing device.
2. The same projectors can be used for centering and focussing of the prime-focus instruments (Section 5.3).

Details of this device are discussed below.

An alternate approach would be to mount a small reimaging projector rigidly to the center of the secondary mirror. A small spot is imaged at the prime focus, which is returned by a spherical dish at the center of the primary mirror and imaged on a quadrant sensor in the projector. This method was applied in the 65-cm photoheliograph (Ref. 5.6) and would be compatible with both the geometrical-optical and the interferometric focus-sensing methods (it could share the spherical primary-mirror insert with the latter), provided interference with the offset plug in the secondary mirror could be circumvented, e.g., by making the plug semi-transparent. However, mounting of the projector might present a packaging problem in the as yet undefined arrangement for exchange of the secondary mirror (or mirrors) with prime focus instruments. For this reason, this approach was abandoned.

A third approach would be to mount a reimaging projector on the telescope structure, separate from the mirrors. This simplifies cabling, but requires additional mirror-position sensing and compensation. For this reason, direct attachment of the sensing device to one of the mirrors is preferred.



Centering-Sensing Concept. Two projectors are mounted to the back of the primary mirror, as shown in Figure 5-6. Large focal lengths are needed to project a spot of sufficiently small diameter at the prime focus. Telephoto optics are applied to keep the physical length within convenient limits.

The beams are directed towards the prime focus by mirrors or prisms cemented to the rim of the primary. Prisms may be better in view of thermal gradients that are likely to exist locally. The prism material should closely match that of the primary mirror.

As in the focus-sensing system, the projector beams fully clear the telescope beam at the mirrors, and pass entirely through the field stop at the prime focus. Likewise, there is no interference with the heat-rejection system.

Optics. An optical diagram of the imaging sequence in each of the beams is shown in Figure 5-7 and identifies the location of the aperture and field-defining stops. To accommodate the beams at the secondary mirror in the presence of maximum primary mirror tilt (9.5 mrad), an increase in obscuration is necessary. However, this is not greater than the increase needed for the focus-sensing system.

The light sources envisioned are 905 nm laser diodes or LEDs and the detectors are quadrant silicon photocells. The two X output voltages are subtracted to give an X-centering error signal and summed to produce a coarse despace error signal. The Y voltages provide redundant Y-centering error signals.

Accuracy and Range. The balance between accuracy and range is controlled largely by the magnification between the prime focus image and the quadrant detector. The diameter of the prime-focus field stop is 7.85 mm (6' at $f_1 = -4500$ mm). An acquisition field

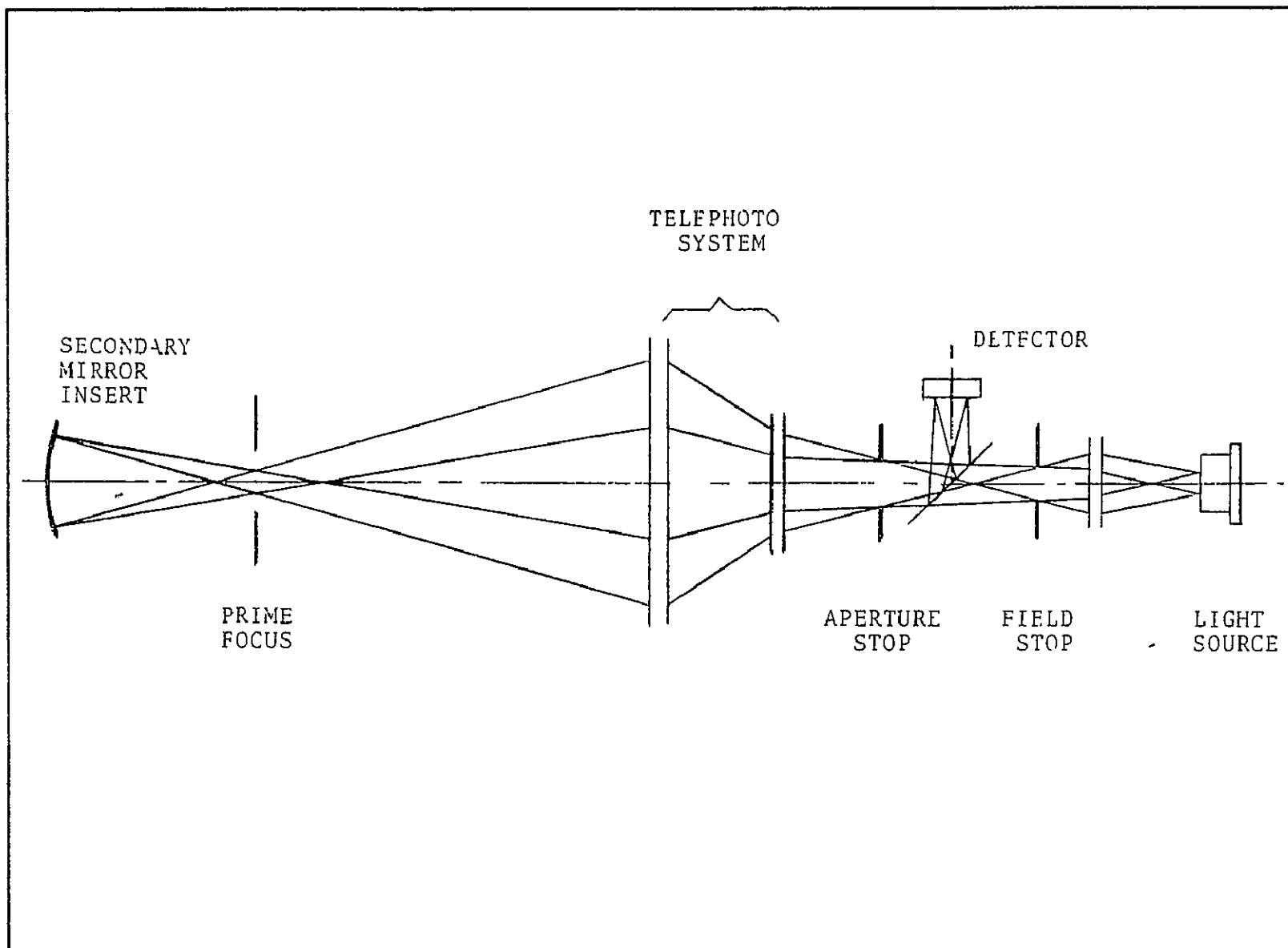


Figure 5-7 Optical scheme of centering-sensing beam



with a radius larger than this diameter is meaningless. Hence, the projected detector diameter should be about 15 mm. By way of illustration, we match this to two different existing detectors, with areas of 2.5 mm x 2.5 mm and 11 mm x 11 mm, respectively (United Detector Technology, Pin Spot/4 and Pin Spot/8). The centering accuracy in each case is listed below and is based on recent laboratory measurements at BBRC. These numbers are almost independent of incident flux in a range of several orders of magnitude and may, therefore, be applied to the case at hand without detailed calculation of the flux levels that can be expected.

Detector size (mm)	2.5	11
Centering accuracy at detector (μm , rms)	3	7.5
Magnification	6	1.5
Centering accuracy at prime focus (μm , rms)	13	8
Associated despace accuracy (μm , rms) (see below)	48	29

Both detectors permit centering within a small fraction of the tolerance. If we apply the criterion that shifts equal to 1% of the image diameter are detectable (Section 5.1.2), we find an accuracy that is even two times better, assuming a reasonable beam diameter (e.g., 60 mm).

We note that the above acquisition range requires initial centering by the primary mirror control system within 3.9 mm (3'), in order to pass the sensing beams through the field stop. This should present no problem if the control actuators are equipped with suitable position indicators.

Coarse Despace Sensing. The coarse despace errors, detectable by the centering-sensing device, are listed in the table above and correspond to focus errors of 2.2 mm and 1.4 mm, respectively, at the gregorian focus. These numbers clearly demonstrate that



separate precise focus sensing at the gregorian focus is indispensable, apart from the fact that the coarse-despace measurement does not include any changes that might occur in the complicated optical train, following the secondary mirror. To assure sufficient overlap with the range of the precision focus-sensing device, the large decenter sensor is preferred (Table 5-1). However, the associated projector optics may be more sensitive to the thermal environment behind the primary mirror.

5.3 FOCUS AND CENTERING SENSING IN PRIME-FOCUS MODE

Under the assumption that an angular resolution of 0.5" is sufficient in the prime-focus mode of operation, the decenter tolerance is 0.5 mm and the focus tolerance $\pm 25 \mu\text{m}$ goal, $\pm 50 \mu\text{m}$ acceptable. As will be shown below, simple image position sensing is amply adequate for centering, but only marginally so for focussing.

Sensing Concept The method recommended by this study is to place two quadrant silicon detectors on each separate prime focus instrument, and to sense the position of images projected by the two projectors described in Section 5.2.

Conceivably, the two sensors could be placed in the immediate vicinity of the prime focus, with the projector beams passing through the hole in the heat rejecting mirror. However, this places inconvenient constraints on the instrument slit arrangements. In addition, the area is partly illuminated by the sun during most solar observations, which creates a difficult shielding problem. For this reason, the sensors are placed outside the area of the

ORIGINAL PAGE IS
OF POOR QUALITY



heat rejection mirror, as shown in Figure 5-8. The minimum off-axis distance is about 80 mm. This is under the assumption that the heat rejection mirror is large enough to intercept the sun image while the SOT is pointed at one solar radius beyond the limb.

To illuminate the sensors, separate offset light sources are needed in the projectors, as shown schematically by the broken line in Figure 5-6.

The sensors may occasionally be exposed to part of the sun's image. This will not cause damage, provided the sensors are heat-sunk well enough to prevent heating beyond 100°C. Further protection may be provided by the narrow-band 905 nm filters, with which each detector is equipped

Primary Mirror Rotation. As a consequence of the large off-axis distances, the detection system is sensitive to rotations of the primary mirror around the telescope axis. Such rotations are likely to be introduced by the A-frame mount, but are easily eliminated from the focus-centering detection system by subtraction of the two Y signals. In fact, the difference signal may conveniently be used to monitor mirror rotations, as a complement to information provided by transducers on the actuators. The maximum possible rotation is ± 80 mrad ($\pm 4.5^\circ$). Full coverage would require a detector height of 15 mm, but seems hardly warranted. In the following, we will assume that a detector size of 11 mm x 11 mm is adequate.

Accuracy and Range. For the above detector and an effective image diameter of the order of 0.6 mm (3 times the gap between the quadrants), the sensing accuracies and ranges are.

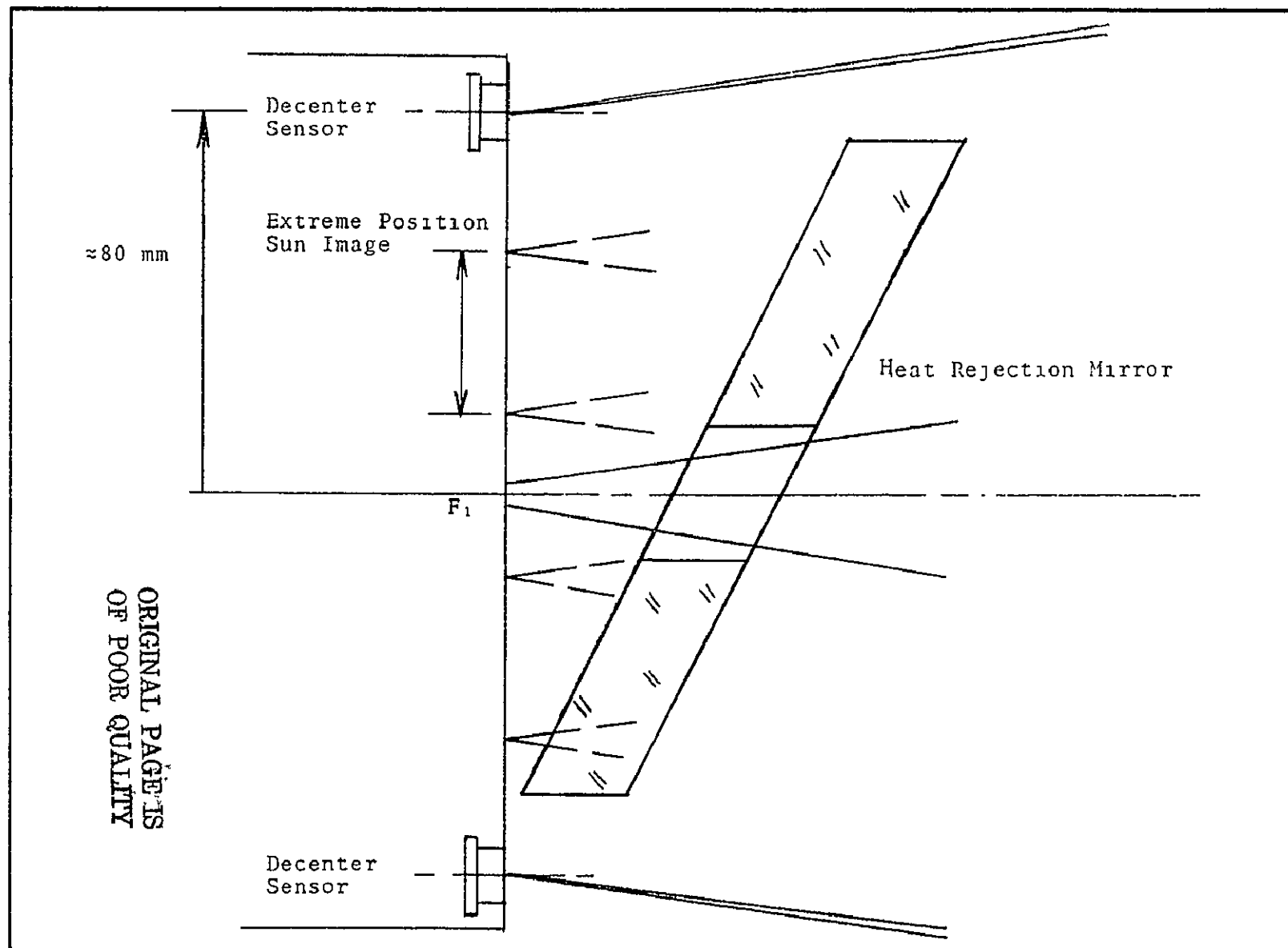


Figure 3-6 Focus and centering sensing at prime focus





<u>Error</u>	<u>Signal</u>	<u>Accuracy (rms)</u>	<u>Linear Range</u>	<u>Acquisition Range</u>
Centering, X	$(X_1 + X_2)/2$	5.3 μm	$\pm 0.3 \text{ mm}$	$\pm 5 \text{ mm}$
Centering, Y	$(Y_1 + Y_2)/2$	5.3 μm	$\pm 0.3 \text{ mm}$	$\pm 5 \text{ mm}$
Focus (axial)	$(X_1 - X_2)f/(2r)$	38 μm	$\pm 2 \text{ mm}$	$\pm 40 \text{ mm}$
Rotation	$(Y_1 - Y_2)/(2h_m)$		$\pm 3.5 \text{ mrad}$	$\pm 60 \text{ mrad}$

The detectable decenter error is of the order of 7% of the tolerance. However, the detectable focus error exceeds the tolerance goal ($\pm 25 \mu\text{m}$) and is only little less than the maximum acceptable tolerance ($\pm 50 \mu\text{m}$). Reduction of the minimum detectable error may be possible if a detector is used with a narrower gap between the quadrants or if the X motion is increased by a negative cylindrical lens, preceding the sensor. This is a matter of later detailed design.

For prime focus operations, focus control must be continuously active, because image motion compensation and rastering are performed by the primary mirror. Hence, there is no need for a margin for drift between corrections.

The linear range is convenient for manual adjusts by the Payload Specialist during initial alignment on-orbit and provides him with a quantitative readout to decide when an alignment update is necessary. For decenter, the range given above equals 6 times the tolerance, but can be increased by selecting a larger image diameter.

For automatic, occasional decenter control, correction may be triggered when the signal reaches preset levels. These levels might even be adjustable during flight, if desirable.



5.4 ACCOMMODATION OF ALIGNMENT SENSING SYSTEMS

The LPS longerons leave a free radius of about 805 mm for accommodation of the primary mirror. This is amply sufficient if the primary mirror diameter is 100 cm. However, if the diameter is 125 cm, the extreme radius for the alignment-sensing accessories may be as large as 800 mm (Table 5-1). In order to allow primary mirror tilts around the prime focus of ± 9.5 mrad (± 45 mm maximum lateral excursion), placement of the accessories near the longerons and the A-frame actuator attachments must be considered in the detailed truss design.

An arrangement that accommodates the above systems is shown in Figure 5-9. This demonstrates that accommodation of the sensing system discussed in the preceding sections, is feasible.

In the geometrical focus sensing system, the primary mirror extensions and the pentaprisms are placed on a line which is offset from the true diameter by 10 or 15 cm. This does not affect operation of the system in any manner, except for a negligible loss in sensitivity.

For the interferometric method, the same arrangement is acceptable, except that the tilt of the central beam with respect to the plane through the marginal beams must be compensated. This can be done by means of a small-angle prism, close to the detector. This prism can also serve as a means for adjustment of the interferometer reference focus and does, therefore, not present an extra complication.

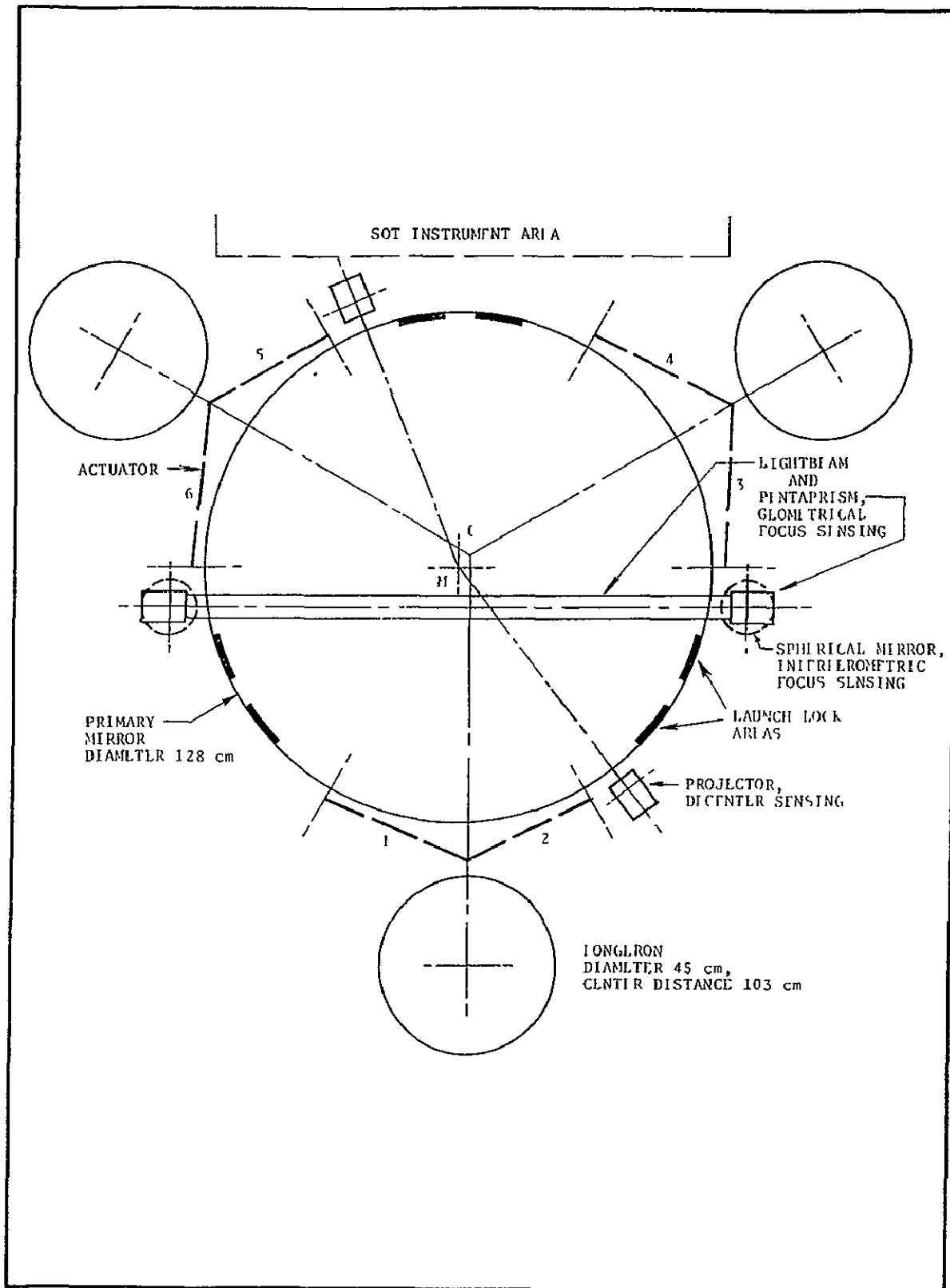


Figure 5-9 Accommodation of alignment sensing system
Mirror center M shown at maximum offset
relative to truss center C.



The projectors for centering and prime-focus sensing are, likewise, offset from the diameter. This introduces a correlation between focus errors and Y-centering errors, which must be resolved by means of an error-signal algorithm. This can be made part of the algorithm already needed to distribute the error signals over the 6 actuators.

The auxiliary mirrors and prisms for the various alignment systems extend locally beyond the boundaries of the LPS, as indicated in Figure 5-9. Thus the alignment system must be considered when assigning space to other LPS facilities. The extreme radii in each of the sensing systems are listed in Table 5-1. These can be reduced only if the sensing optics are allowed to encroach upon the telescope beam. This approach may cause straylight and local heating problems and is not recommended.

ORIGINAL PAGE IS
OF POOR QUALITY



6.0 PRIMARY MIRROR CONTROL MECHANISMS

In Dr. Dunn's concept of the SOT, the primary mirror is supported by 6 rods of adjustable length, which connect 6 equally spaced points at the periphery of the mirror to attach points at the LPS longerons. This so-called "A-frame" mount offers 6 degrees of freedom for mirror control and has been applied to secondary mirror supports in space telescopes by both Itek (Ref. 6.1) and Perkin-Elmer (Ref. 6.2). The latter credits the Franklin Institute with the original invention.

In this section, we investigate the applicability of the A-frame concept to the SOT. The specific aspects considered are:

- Range and resolution of the mirror movements for the various alignment functions.
- Forces on the mirror blank during operation on-orbit, launch/landing and preflight tests on the ground.
- Mechanisms for length control (actuators).
- Coupling of the actuators to the mirror blank. In R. B. Dunn's concept, this is done by means of inserts, mounted directly into the mirror blank.

As will be shown in the following, the A-frame mount is, indeed, suitable for primary mirror control in the SOT, but Dunn's proposed method of actuator attachment needs to be studied in detail. It is not clear that these can be satisfactorily resolved by further analytical studies. It seems best to attack these problems experimentally, (already proposed by Dr. Dunn). An alternate solution would be to place the mirror in a

ORIGINAL PAGE IS
OF POOR QUALITY



cell, as is standard practice in ground-based telescopes. The actuators for this cell could either be arranged in an A-frame configuration or in such a manner that each degree of freedom is controlled by a specific set of actuators. This presents a fully reliable fall-back solution, but is not described in great detail here, since its implementation would not seem to present any uncommon design problems.

6.1 A-FRAME MOTIONS AND FORCES

This section describes the actuator motions necessary for focusing, alignment, offset pointing, and rastering with the primary mirror. We assume an idealized geometrical arrangement, in which the actuators lie in planes tangential to the mirror blank and are attached to the truss at a height equal to the mirror radius r (Figure 6-1). The nominal length of each actuator is then $(2/3)r\sqrt{3}$. This model may not exactly represent the SOT geometry, but is close enough to derive relevant numbers for actuator ranges and accuracies.

6.1.1 Influence Matrix

The length changes in each of the actuators, broken down in terms representing specific alignment corrections, are tabulated in Table 6-1. The coordinate system and the actuator numbers are identified in Figure 6-1. The entry "Rotation" means rotation of the primary mirror around its optical axis. Nulling is desirable to prevent one-directional accumulation of actuator length changes, but is not essential to operation of the A-frame mount. Any 5 actuators suffice to make all alignment corrections, which gives the A-frame mount a high degree of redundancy. This is a desirable feature in free-flying observatories, but is less essential to the SOT. For the present analysis, we limit ourselves to the

Table 6-1
A-FRAME INFLUENCE MATRIX

Length increments in actuators needed for alignment corrections.

Alignment Parameter	Despace	X Decenter	Y Decenter	X Raster	Y Raster	Rotation
Parameter Change	Δd	Δ_x	Δ_y	τ_x	τ_y	ϕ
Actuator						
1	- $\frac{1}{2}\Delta d\sqrt{3} +$	$\frac{1}{4}\Delta_x(2+r/f_1)\sqrt{3} +$	$\frac{1}{4}\Delta_y(2+3r/f_1) -$	$\frac{1}{4}\tau_x(f_1+r)\sqrt{3} -$	$\frac{1}{4}\tau_y(f_1+3\tau) +$	$\frac{1}{2}\phi r$
2	- $\frac{1}{2}\Delta d\sqrt{3} -$	$\frac{1}{4}\Delta_x(2+r/f_1)\sqrt{3} +$	$\frac{1}{4}\Delta_y(2+3r/f_1) +$	$\frac{1}{4}\tau_x(f_1+r)\sqrt{3} -$	$\frac{1}{4}\tau_y(f_1+3\tau) -$	$\frac{1}{2}\phi r$
6-4 3	- $\frac{1}{2}\Delta d\sqrt{3} -$	$\frac{1}{4}\Delta_x(r/f_1)\sqrt{3} -$	$\Delta y +$	$\frac{1}{2}\tau_x r\sqrt{3} +$	$\frac{1}{2}\tau_y f_1 +$	$\frac{1}{2}\phi r$
4	- $\frac{1}{2}\Delta d\sqrt{3} +$	$\frac{1}{4}\Delta_x(2-r/f_1)\sqrt{3} +$	$\frac{1}{4}\Delta_y(2-3r/f_1) -$	$\frac{1}{4}\tau_x(f_1-r)\sqrt{3} -$	$\frac{1}{4}\tau_y(f_1-3\tau) -$	$\frac{1}{2}\phi r$
5	- $\frac{1}{2}\Delta d\sqrt{3} -$	$\frac{1}{4}\Delta_x(2-r/f_1)\sqrt{3} +$	$\frac{1}{4}\Delta_y(2-3r/f_1) +$	$\frac{1}{4}\tau_x(f_1-r)\sqrt{3} -$	$\frac{1}{4}\tau_y(f_1-3\tau) +$	$\frac{1}{2}\phi r$
6	- $\frac{1}{2}\Delta d\sqrt{3} +$	$\frac{1}{4}\Delta_x(r/f_1)\sqrt{3} -$	$\Delta y -$	$\frac{1}{2}\tau_x r\sqrt{3} +$	$\frac{1}{2}\tau_y f_1 -$	$\frac{1}{2}\phi r$



clearly defined case of full rotation correction. However, it should be pointed out that small rotations have an advantage in despace adjusts.. If either the odd or the even-numbered actuators are used exclusively, the length changes needed are twice as large, permitting, in principle, twice the accuracy in despace adjustment.

The decenter factors in Table 6-1 consist of two terms each. One derives from tilt of the primary mirror and the other from a lateral shift. For example, to image an on-axis object point at the first conjugate of the secondary mirror in the presence of a decenter error, Δ_x , a primary mirror tilt, Δ_x/f_1 , is necessary, combined with a lateral displacement $2\Delta_x$ of the vertex. At actuator 1, the first term requires a displacement $(1/2)\Delta_x r/f_s$ in the Z direction, which corresponds to a (negative) length increment $(1/4)\Delta_x(r/f_1)\sqrt{3}$. The second term has a tangential component $\Delta_x\sqrt{3}$ which corresponds to a length increase $(1/2)\Delta_x\sqrt{3}$, as can readily be seen from inspection of Figure 6-1.

The length increments, corresponding to the tolerances of the various alignment parameters, are listed in Table 6-2. Also given are the minimum increments for adequate control. An actuator resolution of 1 μm suffices for despace adjustments within 1/4 of the design goal tolerance, or 1/8 of the largest acceptable tolerance. This resolution is amply sufficient for decenter control also.

For rastering, an accuracy of 0.1" (0.5 μrad) seems desirable, both with regard to the telescope resolution capability at the gregorian focus as to IMC at the prime focus. This requires sub-micron rms accuracies at some of the actuators, which should just be possible with a 1 μm resolution capability. This is especially true if less weight is given to decenter correction (i.e., less

ORIGINAL PAGE IS
OF POOR QUALITY

Table 6-2
 ACTUATORS INCREMENTS CORRESPONDING TO
 VARIOUS ALIGNMENT TOLERANCES

Actuators		1,2	4,5	3,6
<u>Despace</u>		Actuator Increments (μm)		
Maximum Tolerance	10 μm	8.6	8.6	8.6
Design Goal	5 μm	4.3	4.3	4.3
Controllable Fraction	1.25 μm	1.1	1.1	1.1
<u>Decenter, X</u>				
Maximum Tolerance	150 μm	121	139	18
Design Goal	75 μm	60	70	9
Controllable Fraction	22.5 μm	15	17	2.3
<u>Decenter, Y</u>				
Maximum Tolerance	150 μm	59	91	150
Design Goal	75 μm	30	43	75
Controllable Fraction	22.5 μm	7	11	22
<u>Raster, X</u>				
Accuracy, rms	0.5 μrad	0.84	1.11	0.27
<u>Raster, Y</u>				
Accuracy, rms	0.5 μrad	0.33	0.80	1.13



gain in the control loop), which means that accurate image positioning is obtained at the expense of a minute decenter error. The above justifies a baseline actuator resolution capability of 1 μ m as adequate for all alignment functions.

The actuator range is entirely set by the requirement for a rastering amplitude equal to the sun's diameter ($\tau = \pm 9.5$ mrad). For actuators 3 and 6, this means a range of ± 21.3 mm. To allow for slightly different A-frame geometries, we assume an actual range of 50 mm total.

6.1.2 Forces on Mirror Blank

The forces on the mirror blank, induced by the A-frame mount, are calculated for the 1-g environment (testing and integration), as well as the launch, landing and crash environments, specified for Spacelab (Ref. 6.3). First, general expressions are derived for the maximum actuator forces under combined axial and radial loads.

Axial Load. Because of the kinematic design of the A-frame mount, it is justified to assume that an axial load L_z , acting at the center of gravity (c.g.) of the blank, is reacted by equal forces at the actuators. These are then given by

$$F_{z,j} = (1/6)L_z / (\frac{1}{2}\sqrt{3}) = (1/9)L_z\sqrt{3} \quad (j=1, \dots, 6) \quad (6.1)$$

Radial Load, X Direction. For the A-frame geometry of Figures 5-9 and 6-1, the force components for a load L_x at the c.g. can be shown to be

$$F_{x,1} = -F_{x,2} = F_{x,4} = -F_{x,5} = (1/3)L_x\sqrt{3}, \quad (6.2)$$

$$F_{x,3} = F_{x,6} = 0. \quad (6.3)$$



This can be proven rigorously by the conditions that the sum of all Y and Z force components and the moments around the three axes are zero.

Radial Load, Y Direction. Similarly, for a load L_y at the c.g., we find

$$F_{y,1} = F_{y,2} = F_{y,5} = F_{y,6} = (1/3)L_y \quad (6.4)$$

$$F_{y,3} = F_{y,4} = -(2/3)L_y. \quad (6.5)$$

Lateral Load, General Direction. On the basis of the above equations, the forces induced by a radial load L_r in a direction ϕ with respect to the Y axis can be represented by

$$F_{r,1} = F_{r,4} = (2/3)L_r \sin(\phi + 30^\circ) \quad (6.6)$$

$$F_{r,2} = F_{r,5} = (2/3)L_r \sin(-\phi + 30^\circ) \quad (6.7)$$

$$F_{r,3} = F_{r,6} = (2/3)L_r \sin(\phi - 90^\circ) \quad (6.8)$$

From this, the maximum force in any actuator, for a radial load L_r in any arbitrary direction, follows to be

$$F_{r,j,\max} = (2/3)L_r \quad (j=1, \dots 6) \quad (6.9)$$

Compound Load. For the combination of an axial load L_z and a radial load L_r , the maximum force in each actuator is

$$F_{j,\max} = (1/9)|L_z|\sqrt{3} + (2/3)|L_r| \quad (j=1, \dots 6) \quad (6.10)$$



This equation may not represent exactly the forces in the actual A-frame, but is sufficiently accurate for an estimate of the stresses in the mirror blank. One could consider designing the A-frame such that the compound force becomes a minimum for the launch-load conditions to which the SOT will be subjected.

The forces under various environmental conditions are listed in Table 6-3. The launch and landing load factors are derived from reference 6.3, which predicts a maximum "lateral" factor 1.25 and a maximum "vertical" factor 2.8. Because of the as yet undefined orientation of the SOT with respect to Shuttle vertical, we assume a maximum compound radial factor 3.1.

For qualification tests, the launch-environment factors must be multiplied by 1.5. The resulting forces are also given in Table 6-3.

Capability for survival of crash landings is not a prerequisite for admission of the SOT to the Shuttle, provided the debris can be safely contained. However, survival capability should be designed into the launch locks, if at all possible. The forces on the actuators, if not protected by launch locks, are listed in Table 6-3. These are not excessively larger than the compound forces in qualification tests for normal launch and landing. The radial crash load factor (4.7) is the composite of the specified lateral factor (1.5) and vertical factor (4.5).

6.2 INSERTS IN PRIMARY MIRROR

In R. B. Dunn's concept, the actuators are attached directly to the mirror blank by means of metal inserts, secured by a row of locking rings (Figure 6-2). Compared to a conventional mirror

ORIGINAL PAGE IS
OF POOR QUALITY

Table 6-3
FORCES IN A-FRAME ACTUATORS

Mirror Diameter (cm)	100		125	
Blank Diameter (cm)	102		128	
Thickness (cm)	17		21.3	
Mass (kg)	347		685	
<u>Ground Testing</u>	N	(Lb)	N	(Lb)
Force, Telescope Vertical	656	(149)	1294	(293)
Max Force, Telescope Hor.	2271	(514)	4480	(1015)
<u>Launch/Landing</u>				
Max Axial Load Factor 3.3				
Max Force, Axial Load	2165	(490)	4270	(967)
Qualification, Axial Load	3248	(735)	6405	(1451)
Max Radial Load Factor 3.1				
Max Force, Radial Load	6964	(1574)	13737	(3105)
Qualification, Radial Load	10446	(2361)	20606	(4657)
Max Force, Compound Load	9129	(2063)	18007	(4070)
Qualification, Compound Load	13694	(3095)	27011	(6105)
<u>Crash Landing</u>				
Max Axial Load Factor 9.0				
Max Force, Axial Load	5904	(1334)	11646	(2632)
Max Radial Load Factor 4.7				
Max Force, Radial Load	10772	(2438)	21251	(4803)
Max Force, Compound Load	16676	(3772)	32897	(7435)

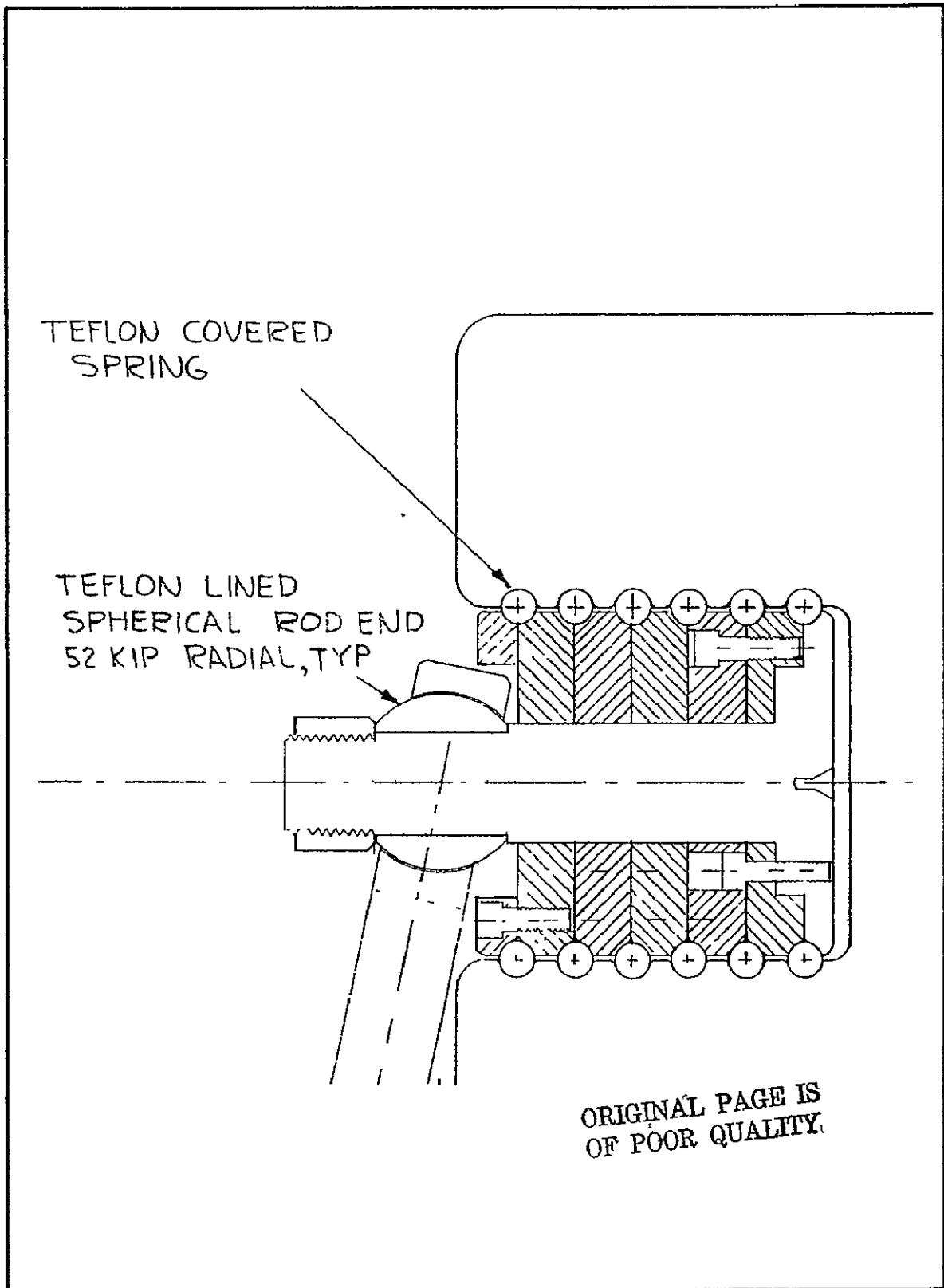


Figure 6-2 Insert in primary mirror for actuator attachment



cell, this saves mass and also space around the mirror. In addition, clamps at the thermally sensitive front surface are avoided. There are two distinct disadvantages, however:

1. The stiffness of the mount depends entirely on the elastic properties of the locking rings, in contrast to conventional mounts, in which the mirror is seated on three virtually incompressible "hard points."
2. The actuator forces act directly on the blank and may distort the mirror figure.

The factors that control these properties are discussed in the following sections. Also considered is a modified insert, in which the above problems are alleviated.

6.2.1 Actuator Reaction Forces at Locking Rings

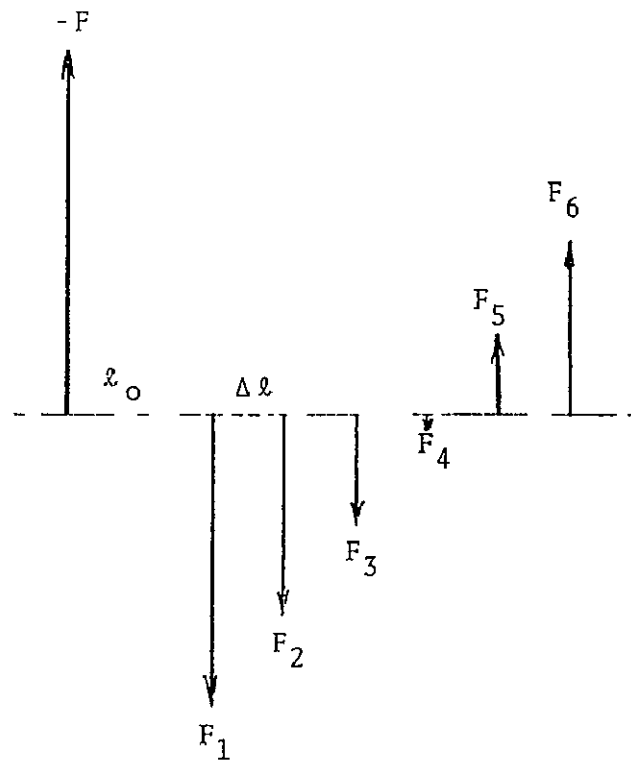
The actuator force F is reacted by forces F_j at the locking rings as shown in Figure 6-3. If we assume that the reaction forces are proportional to the compression of each locking ring for an infinitesimal tilt of the metal core, the following equations apply:

$$F = \sum_{j=1}^n F_j \quad (6.11)$$

$$o = \sum_{j=1}^n \ell_j F_j \quad (6.12)$$

$$l_j = a \ell_j + b \quad (6.13)$$

where ℓ_j is the distance from the j -th ring to the actuator and a and b are constants. The solution of these equations is



$l_0/\Delta l$	1.3	2	3
F_1/F	0.711	0.810	0.952
F_2/F	0.493	0.552	0.638
F_3/F	0.276	0.295	0.324
F_4/F	0.058	0.038	0.010
F_5/F	-0.160	-0.219	-0.305
F_6/F	-0.377	-0.467	-0.619

Figure 6-3 Reaction forces at equally spaced locking rings



$$b = F / \sum_{j=1}^n (1 - C\ell_j)^2 \quad (6.14)$$

$$a = -bC \quad (6.15)$$

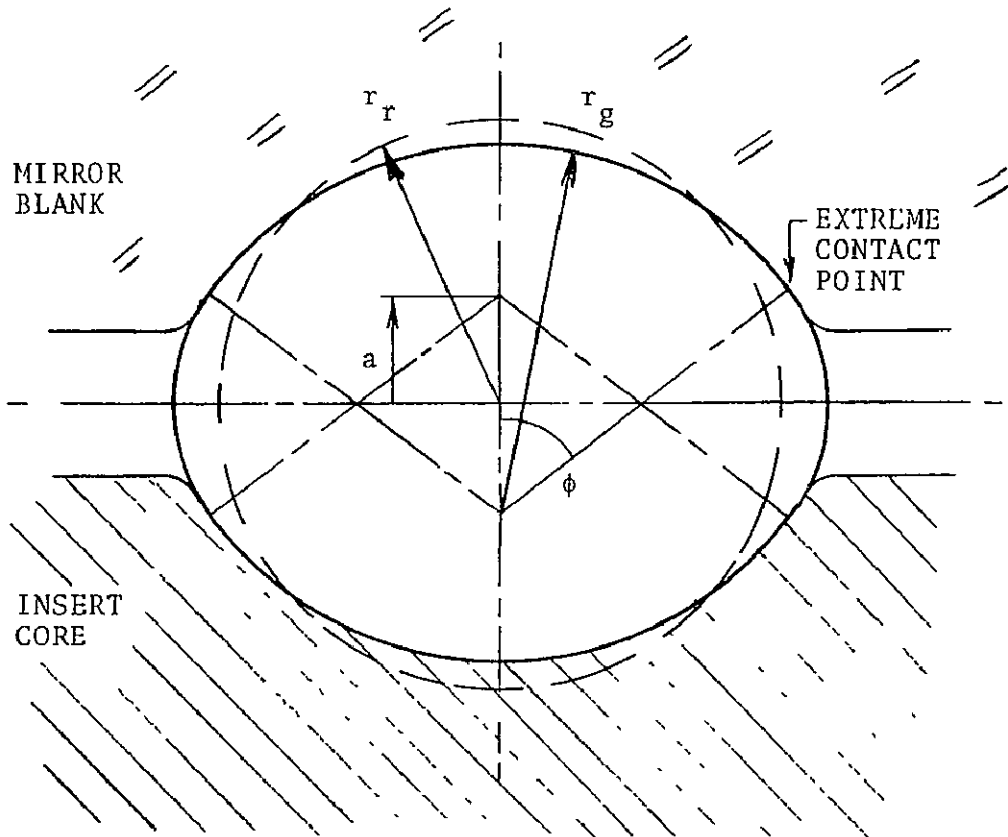
$$C = \left(\sum_{k=1}^n \ell_k \right) / \left(\sum_{k=1}^n \ell_k^2 \right) \quad (6.16)$$

For equally spaced locking rings, a and b depend only on the number of rings n and on the ratio of ℓ_1 to the ring spacing $\Delta\ell = \ell_2 - \ell_1 = \ell_3 - \ell_2$, etc.

The largest reaction force occurs at the first locking ring, which is at the most vulnerable position with regard to loading of the blank material. Numerical examples are given in Figure 6-3. These show that F_1 is only a little smaller than F and does not depend very strongly on the ratio $\ell/\Delta\ell$. The latter eliminates the need of mounting the actuator very close to the blank. The examples in Figure 6-3 apply to $n = 6$. The data for $\ell_0/\Delta\ell = 1.3$ correspond to R. B. Dunn's design, shown in Figure 6-2. For $n = 4$, F_1/F is larger than 1 for all $\ell/\Delta\ell$ values in Figure 6-3. In the following, we assume, for simplicity, $F_1 \approx F$.

6.2.2 Stiffness of Locking Rings

As indicated in Figure 6-4, the locking rings are assumed to be compressed radially, but free to expand in the axial direction. This is necessary to avoid volume compression, which might cause extremely high local stresses. Only relatively small axial loads will occur, because the actuators are almost tangential to the blank (e.g., within 12°).



ORIGINAL PAGE IS
OF POOR QUALITY

Figure 6-4 Cross section of compressed locking ring



The achievable stiffness depends largely on the precision with which the cross-sectional radius r_r of the locking ring can be matched to the radius r_g of the groove. Presumably, the groove can be machined with great precision, but some irregular deviations may result from subsequent etching, which must be done rather thoroughly to eliminate any microcracks. Hence, the difference $r_g - r_r$ must be finite. However, the smaller this difference, the smaller the compression distance needed to establish full area contact between the groove and the ring, i.e., the greater the stiffness.

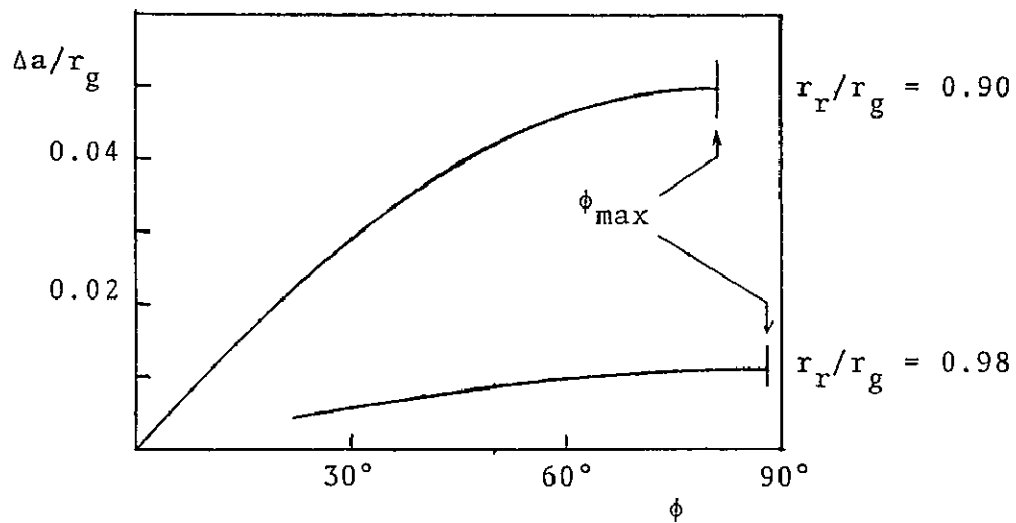
An estimate of the compression distance can be derived from the change in the separation $2a$ of the centers of the grooves in the blank and the core (Figure 6-5). If we assume that the free boundary of the locking ring is circular, the area of the cross section is given by

$$2[\phi r_g^2 - a^2 \tan \phi + (\pi/2 - \phi)(r_g - a/\cos \phi)^2] = \pi r_r^2 \quad (6.17)$$

where ϕ is the angle of the contact point. This equation is based on the assumption that the cross-sectional area of the ring does not change, i.e., the mean ring diameter $2R$ remains the same and the ring material is incompressible. For $\phi = 0$, $a = r_g - r_r$. The relative compression,

$$\Delta a/r_g = [a(\phi) - (r_g - r_r)]/r_g \quad (6.18)$$

is shown in Figure 6-5 as a function of ϕ for two ratios r_r/r_g .



ORIGINAL PAGE IS
OF POOR QUALITY

Figure 6-5 Relative compression distance $\Delta a/r_g$ as function of contact angle ϕ



The total compression range is $0.050 r_g$ for $r_r/r_g = 0.90$, but only $0.011 r_g$ for $r_r/r_g = 0.98$. The absolute range is proportional to r_g , i.e., the thinner the locking ring, the smaller the compression range. A practical lower limit might be $r_g = 2.50$ mm, and $r_r = 2.45$ mm. This would give an absolute range $\Delta a = 28 \mu\text{m}$.

The stress distribution associated with compression of the locking ring is shown schematically in Figure 6-6. If the core is moved over a distance dz by a force F_1 , the compression Δa , as a function of ϕ , changes by $(1/2)dz\cos\phi$. The associated additional stress $\bar{S}_1\cos\theta$ is related to F_1 by

$$F_1 = \int_0^{2\pi} \bar{S}_1 \cos\theta w R \cos\theta d\theta = \pi R w \bar{S}_1 \quad (6.19)$$

where w is the effective width of the ring and R its mean radius. We point out that \bar{S}_1 is the average stress across w .

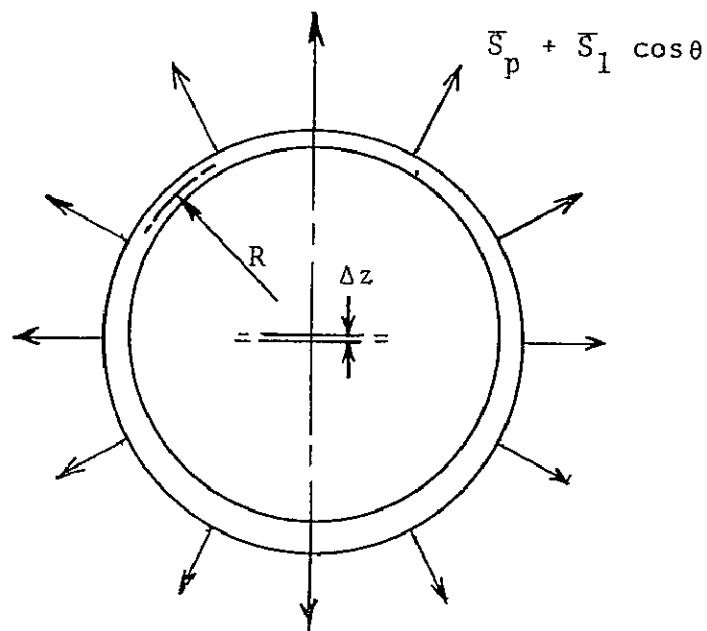
The exact relation between \bar{S}_1 and dz is difficult to predict and depends entirely on the elastic properties of the ring material. However, an estimate of the preload stress \bar{S}_p (averaged over w) can be made if we make the highly simplified assumption

$$2\bar{S}_1/dz \approx \bar{S}_p/\Delta a \quad (6.20)$$

From this, it follows that the stiffness, defined as F_1/dz , is approximately given by

$$F_1/dz = (\pi/2) R w \bar{S}_p / \Delta a \quad (6.21)$$

This allows a rough estimate of the preload, needed to create the necessary stiffness. For normal operation on-orbit, this can be done as follows: The IPS is expected to provide a pointing



ORIGINAL PAGE IS
OF POOR QUALITY

Figure 6-6 Stress distribution at locking ring

C-2



accuracy $\psi \approx 1''$ rms, with a bandwidth ν of a few Hz. If we assume that the c.g. of the SOT lies at a distance $d_c \approx 3$ m in front of the primary mirror (mass $M = 650$ kg), the induced loads in the actuator are of the order of

$$F_{1,rms} = (2/3)(2\pi\nu)^2 M d_c \quad (6.22)$$

If we assume $\nu = 5$ Hz as a worst case, we find $F_{1,rms} \approx 6$ N rms. The occasionally occurring maximum force F_1 is then of the order of 20 N (3σ). If we require $dz \leq 1$ μ m (the actuator accuracy, established in Section 6.1), and assume as before, $r_g = 2.5$ mm and $r_r = 2.45$ mm, we find, e.g., $Rw\bar{S}_p \approx 360$ N (80 lb).

The resonance frequencies of the mirror in the A-frame mount are entirely determined by the stiffness of the inserts. By way of example, we consider a simple oscillation in the axial direction. The restoring force is then equal to $6 dF_1/dz$, which amounts to 12×10^7 N/m for the numerical data in the preceding paragraph. The resonance frequency ν_v is then about 70 Hz, as follows from the relation

$$(2\pi\nu_v)^2 = 6(dF_1/dz)/M \quad (6.23)$$

This frequency is sufficiently high to allow control time constants of the order of 0.1 sec, as well as suppression of high-frequency oscillations, spuriously transmitted by the IPS.

6.2.3 Stresses in Mirror Blank

The maximum stresses at the surface of the insert cavity can be estimated from Eq. (6.21) in combination with the empirical rule $\Delta\alpha \approx 1 - (1/2)r_r/r_g$, justified by the data in Figure 6-5, and by



the assumption that the effective width is about 2/3 of the ring thickness, i.e., $w = 4/3 r_g$. The latter is based on a quadratic stress distribution across the width, which is zero at the extreme contact points. This leads to the equation

$$S_{1,\max} \approx (3/\pi) F_1 dz / [R r_g (r_g - r_r)] \quad (6.24)$$

For example, if we assume $R = 40$ mm, in addition to the numerical data used before, we find $S_{1,\max} \approx 1.8 \times 10^6 \text{ N/m}^2 = 260 \text{ psi}$. According to Reference (6.4), this is about half the stress that should conservatively be admitted in primary mirror slabs to assure that only fully recoverable elastic strain does occur. Because the material is loaded in tension, it seems wise to adhere to this rule.

The above does not imply that mirror surface deformations do not occur. However, serious deformation seems unlikely, since the insert is located near the neutral zone and lies at least 6 cm below the mirror surface. Detailed stress analysis by computer or by experimental investigation would be necessary to provide an unambiguous answer to this question and lies beyond the scope of this study.

In preflight testing, the actuator forces are at least an order of magnitude larger than the 20 N force, estimated for operation on-orbit (Table 6-3). This means that rings, optimized for flight, would collapse or, if the rings were designed to withstand the 1-g forces, the stresses in the blank might become dangerously high. It should be pointed out, however, that stresses up to 2000 psi are accepted for general applications of CerVit and ULE (Ref. 6.4). One solution of this problem would be to support the mirror by means of auxiliary springs during testing, which would not be too difficult if testing is done vertically.



6.2.4 Launch Locks

From the foregoing, it is quite obvious that launch locks are indispensable for protection of the inserts as well as the mirror blank during launch and landing. Launch locks can be accommodated at the rim of the mirror in the three areas not occupied by the alignment optics, as shown in Figure 5-9. Each lock could exist of a fixed resilient seat in front of the mirror, against which the mirror is pressed by a padded actuator. The actuators could consist of ball-bearing screws, driven by synchronously pulsed stepper motors. This would assure simultaneous operation. The locks must provide support in all radial directions as well as positive and negative axial directions. Furthermore, the pads must be large enough to maintain launch-induced stresses at acceptable levels.

An estimate of the support areas needed can be made by assuming that the qualification loads in Table 6-3 should not cause a stress greater than 500 psi ($14 \times 10^6 \text{ N/m}^2$). This leads to the following dimensions

Mirror Diameter:	100 cm	125 cm
Axial Support Area:	3 x 16 cm ²	3 x 32 cm ²
Radial Support Area:	3 x 15 cm ²	3 x 30 cm ²

To accommodate the axial support area, the mirror must be provided with a flat rim, e.g., 1 cm wide for the 1-m mirror and 1.5 cm wide for the 125-cm mirror. The length of each support strip then becomes 16 cm and 22 cm, respectively. It is assumed that the strip is divided in two sections and mounted on a swivel-supported bracket. The mirror could be seated pseudo-kinematically and the stresses would be spread out over a reasonably large portion of the rim. This is illustrated in Figure 5-9.



For radial clamping, ample area is available at the sides of the mirror blank. Design of the radial clamps must allow them to be completely withdrawn to allow free scanning through a range of $\pm 0.5^\circ$.

During launch, the total forces on the mirror are composed of the launch loads and the preloads of the locks. If the latter are of the order of 2 or 3 g, the actual stresses experienced by the mirror are still less than 650 psi, which is a factor of 3 below the level permitted for CerVit (Section 6.2.3). This also indicates that crash loads could safely be absorbed.

Before the launch locks are applied, it is necessary to decouple the actuators from the mirror inserts, as is discussed in more detail in Section 6.3.3. Also, the mirror must be moved close to its center position. The actual design of the launch-lock system must compensate for possible actuator failure prior to preparation for reentry and landing.

6.2.5 Alternate Insert Concept

Possible problems with the insert concept of Figure 6-2 can be summarized as follows:

- Extremely high preloads may be necessary for adequate stiffness.
- The groove profiles in the core must be matched precisely with those of the individual grooves in the blank.
- Accurate and reliable operation in preflight testing cannot be guaranteed.

ORIGINAL PAGE IS
OF POOR QUALITY



An alternate concept which may eliminate these difficulties is shown in Figure 6-7. The insert is held in contact with the blank at "hard points" A_1 and B_1 and kept in place by spring plungers A_2 and B_2 . Of course, a similar retaining system is needed in the orthogonal direction. Alternatively, an arrangement of 2 hard points and 1 spring plunger at 120° in each of the planes through A_1 and B_1 could be employed.

Obviously, the hard points must be carefully contoured to match the curvature of the cavity. This may be easier than manufacturing the intricate grooves in the earlier concept. In this concept a great degree of freedom exists in the selection of pad dimensions and materials to assure a uniform load distribution across the pad, combined with high stiffness in the load direction.

The stresses in the blank can be estimated as follows: If F is the actuator force, the reaction at A_1 is of the order of $2F$, and at B_1 of the order of $-F$. On-orbit, F can be either positive or negative. The retaining force at A_2 should, therefore, be well in excess of $2F$, say $4F$. The maximum possible load at A_1 then becomes $6F$. Using the estimate of on-orbit forces in Section 6.2.2 (i.e., $F \approx 20$ N max), we find a maximum pad load of 120 N. This means that a pad diameter of 7 mm would be adequate to keep the stress below the desired level of 500 psi.

As is evident from Figure 6-7, there should be no problem in making the pad diameter much larger, e.g., 25 mm. This would enhance the feasibility for safe and accurate operation in a 1-g environment. If the hard points are oriented such as to carry directly the weight of the blank, the small retaining forces needed for operation on-orbit (80 N max) remain adequate. The stresses incurred under these conditions can be derived from Table 6-3 and are listed below.

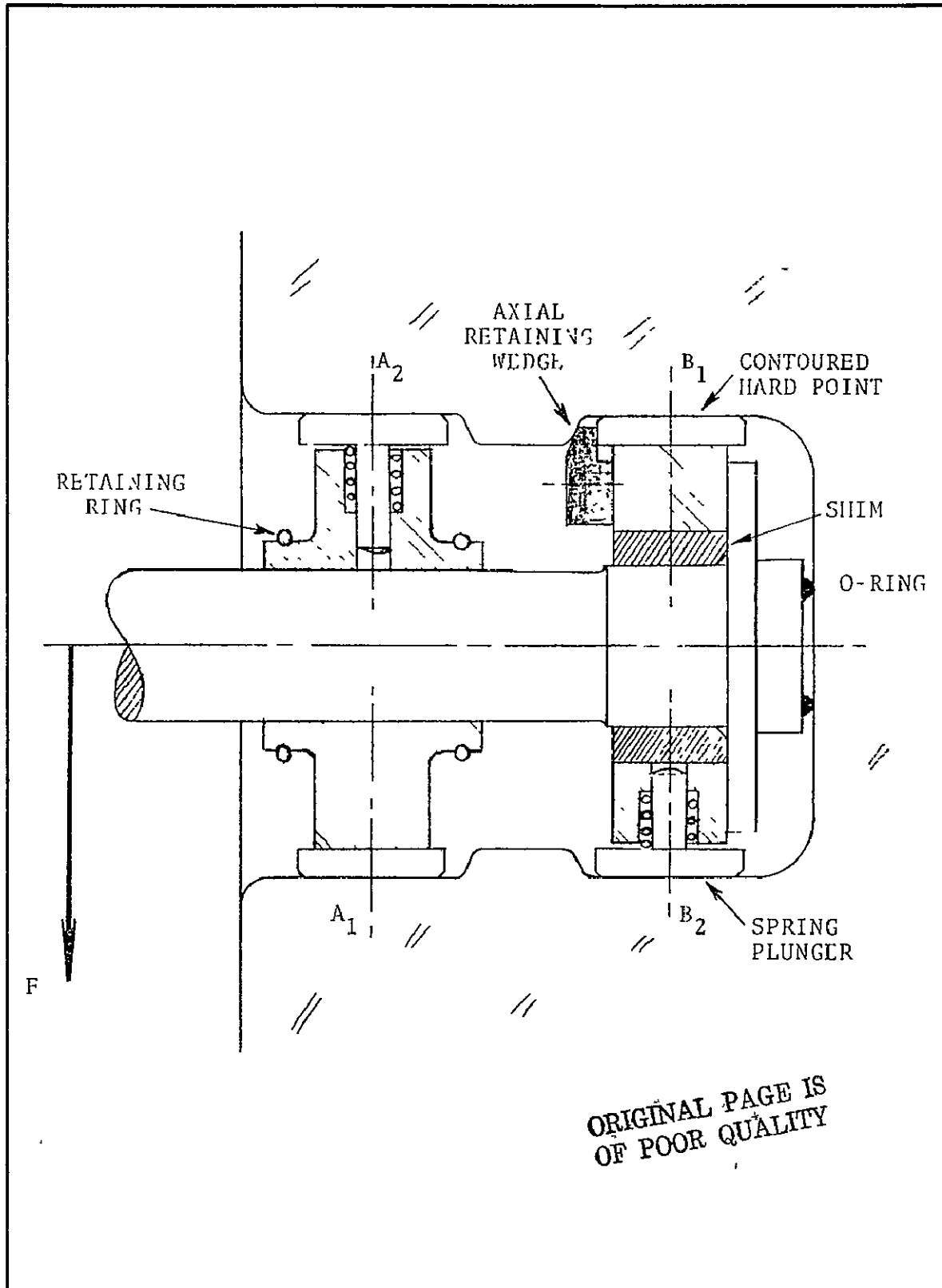


Figure 6-7 Hard-contact mirror insert



Mirror Diameter:	100 cm	125 cm
Stress in Vertical Testing:	415 psi	795 psi
Stress in Horizontal Testing:	1375 psi	2690 psi

This indicates that safe testing of the 1-m mirror is possible in both vertical and horizontal positions, if we accept a minimum permitted stress level of 2000 psi. For the 125-cm mirror, only vertical testing would seem possible, but further enlargement of the pads might be feasible if horizontal testing would become mandatory.

To assemble the insert in the cavity, Figure 6-7 assumes that first the shaft and its end flange are put in, whereupon the hard points and plunger units B_1 , B_2 , etc. are slid past the ridge in the cavity and spread out by shims. These elements are then all bolted to the flange or secured by other means (no details shown). The thickness of the shims can be selected to adjust the preload in the plungers. The shaft is locked axially by an O-ring at the end and resilient wedges between the hard points and the cavity ridge. Care must be taken to make the contact areas large enough to safely accommodate axial loads on-orbit and in preflight testing. Finally, the units A_1 , A_2 , etc. are slid in place and secured. These units do not carry an axial load. Simple devices (e.g., locking rings) suffice.

The above demonstrates that insert designs are feasible, which offer high stiffness, combined with low stresses, in the same manner as the classical external mirror mount. Various ways of implementation can be conceived, but will not be explored further in this study.



6.3 ACTUATORS

Prior to the mid-term review, various actuator concepts were evaluated. Simultaneously, the requirements in terms of range, accuracy and load capacity were developed. The results of this work were presented in the mid-term review. During the ensuing discussions, one particular actuator system was identified as most suitable for the SOT. This concept was subsequently worked out in detail by R. B. Dunn and made available for inclusion in this report. Before we describe this actuator, the considerations that led to its selection will be briefly recapitulated.

6.3.1 Selection of Actuator Concept

The candidate actuators mechanisms considered early in the study can be divided into two categories; namely, those that use flexures and those that use bearings to support the load-carrying members.

Flexures have the advantage of extremely high reproducibility (zero backlash), coupled with noise-free operation, even under high loads. However, the range is usually rather limited. Flexures are applied, for instance, in a secondary mirror control system, developed by Perkin-Elmer for the Space Telescope (ST). Application in the SOT was favored initially but was abandoned when the rastering range, originally assumed to be only 8', was firmly established at ± 10 solar diameter in the mid-term review. There was also the complication that the actuator in the A-frame is subjected to small torques around its axis, which require either torsional flexibility of the actuator or a universal flexure joint at one of the attach points. Furthermore, the flexures subject the mirror insert to additional torque loads. We note that both objections disappear if the actuator is used in combination with a mirror cell, as is the case in the ST.

ORIGINAL PAGE IS
OF POOR QUALITY



Bearing-type mechanisms that offer both the range and the load capacity needed include:

- Conventional lead screws
- Linear harmonic drives
- Ball-bearing screws

The selection from these was based on the specific requirements for the case at hand; i.e., a range of 50 mm, a resolution of 1 μ m (Section 6.1.1) and worst-case loads of 4500 N (1015 lb). The latter number applies to horizontal preflight test of the telescope equipped with the 125-cm mirror (Table 6-3). This requirement was maintained regardless of the question whether the mirror insert could indeed carry such a load.

Lead Screw. The conventional lead screw offers the resolution capability under no-load conditions, but has high friction and wear. It has been successfully applied in short duration rocket telescopes, however (Reference 6.5), and might be adapted to prolonged flights by proper lubrication; e.g., BBRC's VacKote.

Linear Harmonic Drive. This device has been applied by Itek in an engineering model of the A-frame mount for the secondary mirror of the ST (Ref. 6.6). The actuator had a static load capacity of 1300 N (300 lb) and an operating capacity of 110 N (25 lb). The resolution capability was about 10 microns, but the actual units built showed an unexpected hysteresis effect. However, this was probably not caused by the harmonic drive, but rather by the preceding gear head.

Ball Bearing Screw. By comparison, the ball bearing screw offers the best potential for meeting all requirements. It combines high load capacity with low, rolling friction and low wear. High resolution is possible with proper preloads. A potential



disadvantage is noisy operation. However, during actual observations, mirror adjustments are kept at a minimum, which largely eliminates this objection. In the mid-term review, the ball-bearing screw was, therefore, selected as the basis for further design.

6.3.2 Design of Selected Actuator

Dr. R. B. Dunn's actuator design (dated 5/8/76) is shown in Figure 6-8. The main components are a ball-bearing screw (1) and nut (2), a rotary harmonic drive (4, 5 and 6) and a torque motor (8). A rotary harmonic drive was chosen instead of a gear train to avoid possible backlash in the latter. The unit is sealed by bellows, which also provide the necessary preload. The diameter is about 10 cm, the total length about 40 cm. A linear transducer (10) and an encoder are included to monitor the actuator position. A tachometer (9) is coupled to the torque motor for feedback control.

The actuator has the following characteristics:

- Range 50 mm (2 in)
- Resolution 1 μ m
- Speed 0.16"/sec (12 sec to cross sun)
- Load Capacity 8800 N (2000 lb)
- Stiffness 0.43 μ m at 8800 N load
- Self-locking
- Sealed for contamination containment
- All components off-the-shelf

Clearly, this design meets or exceeds all the criteria established in this study. Also, it can be built in any well-equipped machine shop, and readily be applied in engineering tests.

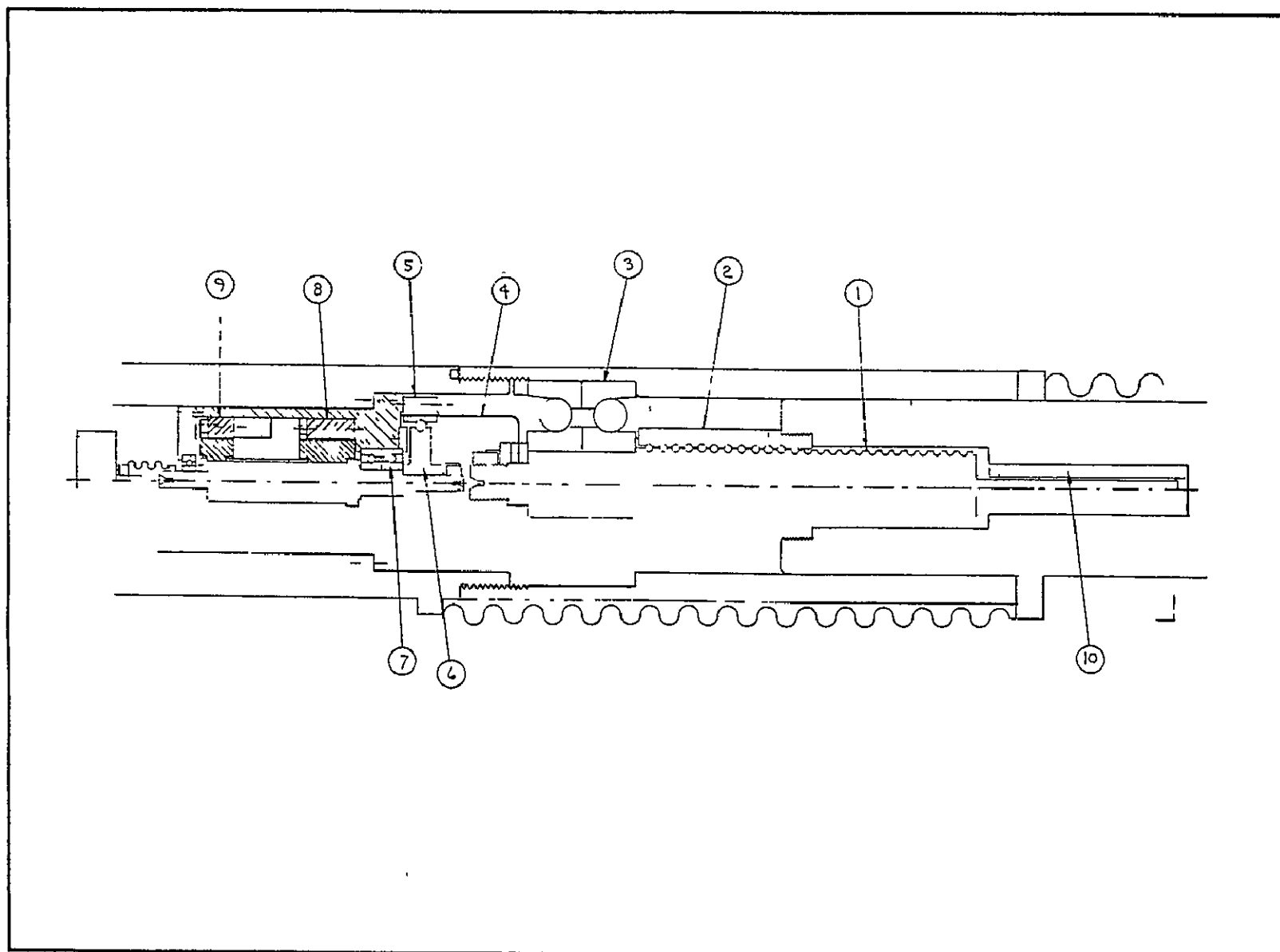


Figure 6-8 Actuator with ball-bearing screw, rotary harmonic drive and torque motor





6.3.3 Mirror-Insert Joint

The joint between the actuator and the mirror insert must meet the following requirements.

- Sub-micron backlash
- Low friction
- 3 degrees of freedom in rotation (2 if the actuator screw is not coupled to the housing by the bellows)
- Release insert when mirror is locked for launch
- Mount sufficiently close to the mirror blank (Section 6.2.1).

This can be accomplished, for instance, by the mechanisms shown in Figure 6-9. The insert carries a perforated ball, which acts as the inner race of a thrust bearing, attached to the actuator rod. A preloaded second bearing assures contact under varying loads in operation on-orbit. The spring load is, for instance, 120 N; i.e., 2 times larger than the maximum load, estimated in Section 6.2.2. In this manner, the first three requirements can be met. However, it remains to be seen whether the static friction is indeed low enough to leave the mirror figure undisturbed after the actuators have stopped operating. This is one of the most important aspects of the engineering tests, planned by Dr. Dunn.

During launch and landing, it is necessary to disengage the mirror from the actuators, to prevent excessive loads on the inserts. This operation can be executed simultaneously with locking the entire mirror (Section 6.2.4). If the mirror is pressed forward by the launch-lock actuators, the thrust bearing is automatically released. The bearing balls are held captive

ORIGINAL PAGE IS
OF POOR QUALITY

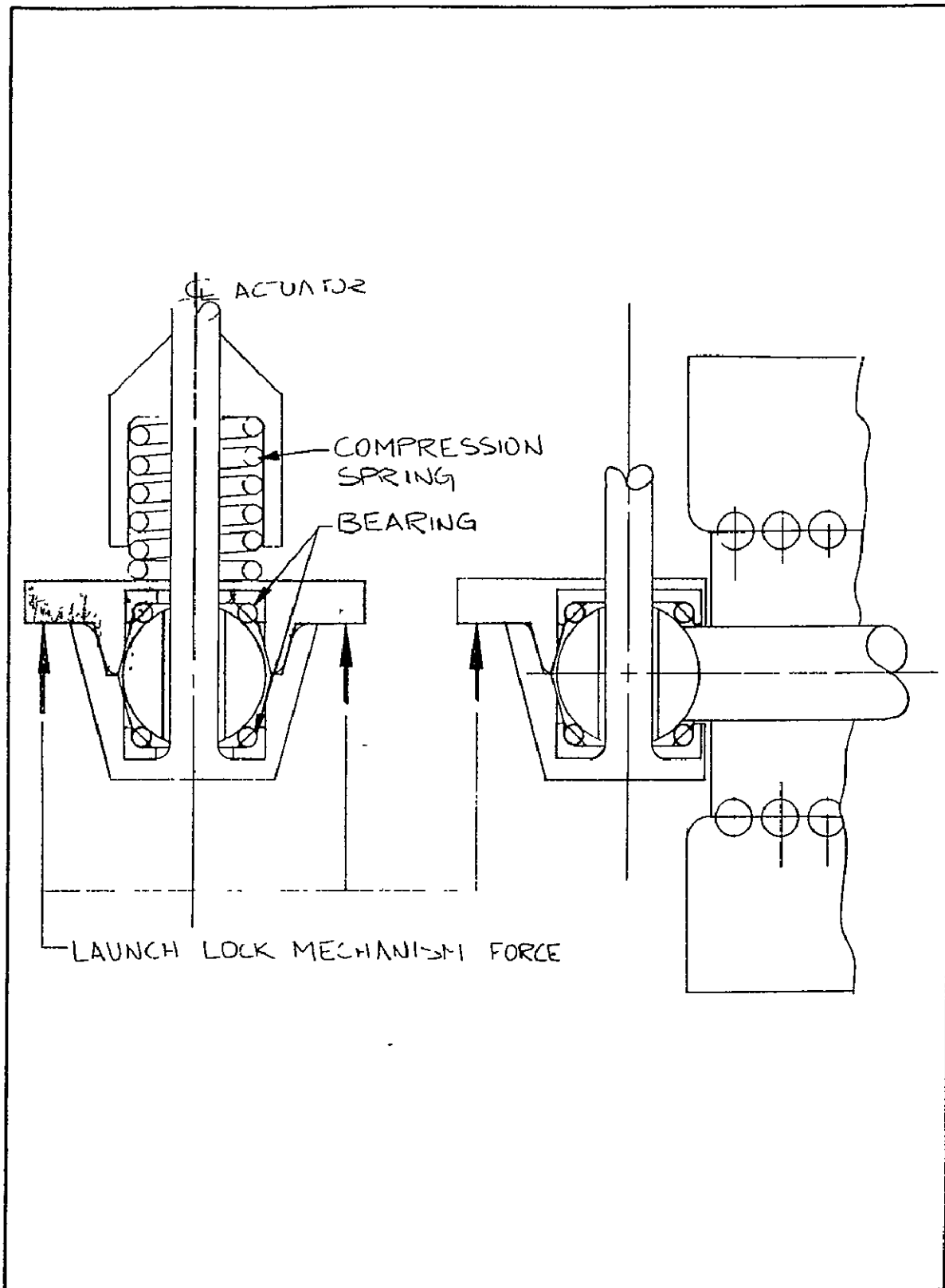


Figure 6-8 Backlash-free actuator joint, detachable during launch and landing



in a cage, which is loosely retained by the fixed race. During launch and landing, only the preload spring then acts on the insert. Even this force can be removed if the mechanism that lifts the mirror also lifts the preload bearing, as indicated by arrows in Figure 6-8. This does not interfere with attachment of the actuator close to the mirror blank.

The above illustrates the feasibility of a backlash-free joint which is immune to the launch and landing environment. It also identifies the complications involved. Undoubtedly, other solutions are possible, but exploration of these must be left to further engineering studies or hardware developments.

ORIGINAL PAGE IS
OF POOR QUALITY



REFERENCES

- 3.1 R. B. Dunn, SOT Optical Design, FDT Note April 26, 1976.
- 3.2 M. Bottema and R. A. Woodruff, Applied Optics, 10, 300 (1971).
- 3.3 Photoheliograph Definition Study (LSO), Itek Report 72-8212-3, January 1973, Volume II, Book I, Section 4.3.
- 3.4 R. J. Wollensak and C. A. Rose, Optical Engineering, 14, 539 (1975).
- 3.5 M. Born and E. Wolf, "Principles of Optics," Pergamon Press 1959, Chapter 9.2.
- 3.6 Reference 3.3, Section 3.2.
- 3.7 W. J. Smith, "Modern Optical Engineering," McGraw Hill, 1966, p. 320.
- 5.1 Photoheliograph Definition Study (LSO), Perkin-Elmer Report 10747A, September 1971, page 16.
- 5.2 J. D. Strong, Applied Optics, 6, 179 (1967).
- 5.3 M. A. Reed, J. Opt. Soc. America, 66, 1092, October 1976(A).
- 5.4 Y. Väisälä, Thesis Helsingfors, 1923.
- 5.5 F. Zernike, J. Opt. Soc. America, 40, 326 (1950).
- 5.6 CIT Photoheliograph Definition Study, BBRC Final Report F71-02, April 1971, Section 5.2.3.
- 6.1 Reference 3.3, Section 9.1.
- 6.2 Space Telescope, Phase B Definition Study, Perkin-Elmer, Optical Telescope Assembly, 1976.
- 6.3 Space Shuttle System Payload Accommodation, Level II Program Definition and Requirements, JSC-07700, Volume XIV, 1974 Change 15, page 7-20.



References continued--

- 6.4 Technology Study for a Large Orbiting Telescope, Itek Report 70-9443-1, May 1970, Appendix D, Section 2.2.
- 6.5 J. W. Gilles, W. R. McKinney, C. S. Freer and H. W. Moos, Space Science Instrumentation 1, 51 (1975).
- 6.6 Space Telescope Optical Telescope, ST/SR&T Mirror Mount System, Itek Final Report, 28 May 1976, Section 4.